ARTICLE | OPEN ACCESS

Discovery

To Cite:
Abdul R, Amangabara GT, Johnbosco U, Ejike DE, Izunobi LC, Umar NA, Victoria EC, Acholonu CA, Ruth JI, Ndagi BU, Abdullahi KI. Crystallographic Analysis and Environmental Fate Modeling of *Moringa Oleifera* Seed-Derived Silver Nanoparticles for Water Purification Applications. *Discovery* 2026; 62: e21d3290
doi:

Author Affiliation:
[1]Dept Environmental Management, Federal University of Technology, Owerri, Nigeria
[2]Department of Chemistry, Federal university of Technology, owerri, Nigeria
[3]Dept. Entrepreneurship and Innovation. Federal university of Technology, owerri, Nigeria
[4]Dept. Petroleum Engineering. Federal university of Technology, owerri, Nigeria
[5]Dept. of Geography, Federal university Lafia, Nigeria

***Corresponding author:**
Rufai Abdul,
Dept Environmental Management, Federal University of Technology, Owerri, Nigeria

Peer-Review History
Received: 07 January 2026
Reviewed & Revised: 30/January/2026 to 30/June/2026
Accepted: 18 July 2026
Published: 30 July 2026

Peer-Review Model
External peer-review was done through double-blind method.

Discovery
pISSN 2278–5469; eISSN 2278–5450

Crystallographic Analysis and Environmental Fate Modeling of *Moringa Oleifera* Seed-Derived Silver Nanoparticles for Water Purification Applications

Rufai Abdul[1]*, Amangabara GT[1], Umunnakwe Johnbosco[1], Duru Erasmus Ejike[3], Izunobi LC[1], Nasir Adamu Umar[1], Ekweogu Chinonye Victoria[1], Acholonu CA[1], Joseph Isah Ruth[2], Baba Usman Ndagi[4], Kasim Ismail Abdullahi[5]

ABSTRACT

This research proposes an integrated framework for crystallographic characterization and environmental fate modeling of the Ag-nanoparticles obtained from *Moringa oleifera* seed extract (Mo-AgNPs) to fill some key knowledge gaps in the responsible use of green nanotechnology for decentralized water treatment. The face centered cubic metallic silver was confirmed through X-ray diffraction analysis and the crystallite size was determined using the Scherrer formula, which was found to be 24.7 ± 3 nm and the crystallinity index was determined to be 92.4%, showing the superior crystalline quality. The Advection-Dispersion-Reaction equation, parameterized using hydrological data from Doma (Nasarawa State, Nigeria), showed evident seasonality dependency of the fate of nanoparticles. Under wet season conditions, dispersal occurred quickly and 5% was left undispersed after 200 days, while dry season conditions showed much more persistence with 60% remaining within 500 m of the source. Slow groundwater transport and moderate persistence were simulated. Bioaccumulation modeling for tilapia and benthic snails showed contrasting organism responses, with bioaccumulation factors of 57Lkg-1 for tilapia and 400Lkg-1 for snails, which would be considered "very bioaccumulative. The exposure estimates through fish consumption (0.03 mg/day) were higher than the WHO provisional tolerable daily intake, suggesting a potential public health problem for the communities with high consumption. Sensitivity analysis indicated that the dominant parameters influencing groundwater fate were degradation rate, and the critical ones for ecological risk assessment were bio-uptake. Based on these findings, evidence-based risk mitigation measures can be implemented, such as encapsulation, immobilization within filter matrices, management practices during the season and targeted ecological monitoring programs to help transition green nanotechnology from discovery in the lab to field-scale implementation with quantified risk and management.

Keywords: Silver nanoparticles, *Moringa oleifera*, crystallographic analysis, environmental fate modeling, bioaccumulation, risk assessment, water treatment

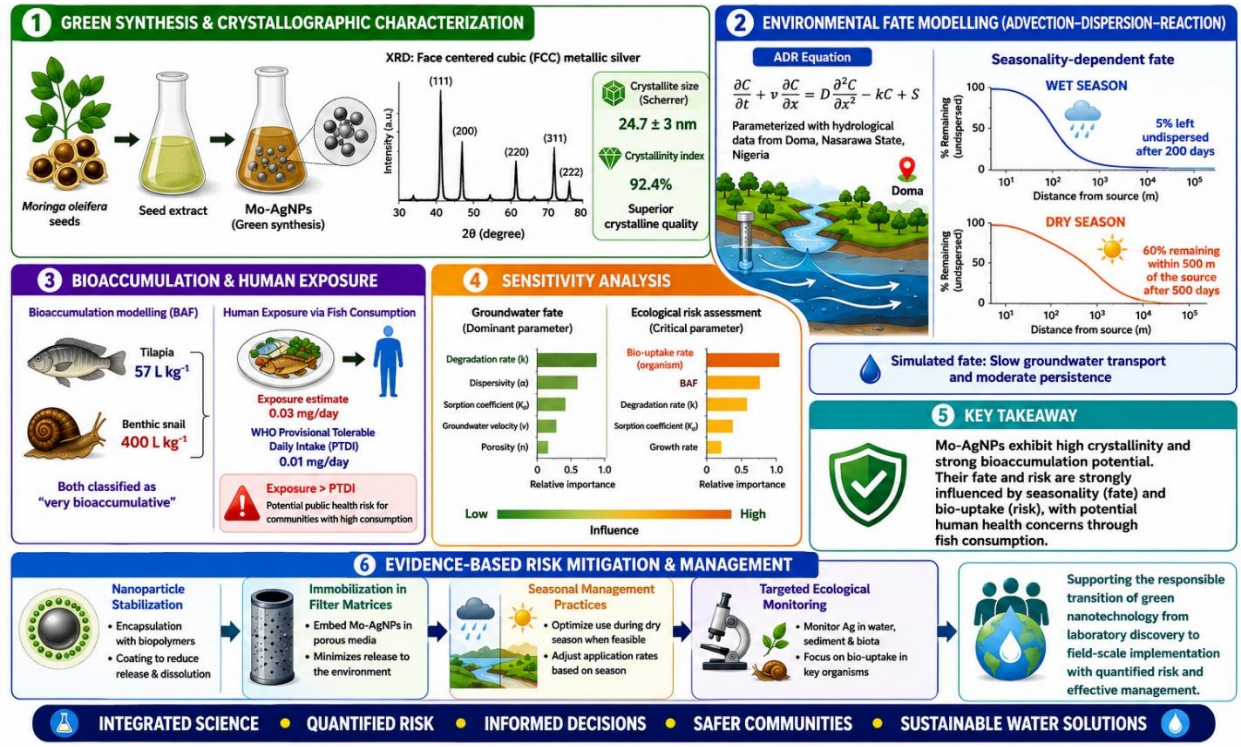

1. INTRODUCTION

Safe and potable water provision continues to be a major challenge worldwide, especially in rural areas of sub-Saharan Africa, such as Doma, Nasarawa State, Nigeria (Rufai et al., 2026). In these regions, the residents often rely on polluted surface water and groundwater, which are increasingly threatened by geogenic pollution, agricultural runoff, sanitation issues, and other factors (Hassan et al., 2025).. The contamination pathways involve the release of pathogenic microorganisms, heavy metals, and a wide variety of organic pollutants which pose a serious public health threat (Coelho et al., 2023). In such resource limited areas, however, traditional centralized water treatment methods such as chlorination and alum coagulation tend to be expensive, energy-intensive and logistically difficult (Mohamed, 2021). Moreover, these processes are also associated with the formation of adverse environmental side-products like toxic metallic sludge and carcinogenic disinfection by-products (Sadia et al., 2025). Due to this crisis, efforts have been made to develop Sustainable and decentralized water treatment technologies (Aouf et al., 2024). The application of natural coagulants, like *Moringa oleifera* seeds, has been proven to reduce wastewater turbidity, to deactivate bacteria, and to precipitate heavy metals from wastewater, which is one of the promising strategies (Pratiwi et al., 2019). With the development of nanotechnology and green chemistry, *Moringa oleifera* seed extracts have been explored as a natural source to synthesize silver nanoparticles (AgNPs), which not only harness the seeds' inherent coagulant property, believed to arise from cationic proteins capable of neutralizing negatively charged colloids but also leverages the seeds' high antimicrobial and catalytic capabilities due to the presence of nanoscale silver.

The Moringa oleifera-derived silver nanoparticles (Mo-AgNPs) have been a critical step forward in the development of bio-nanocomposites for water treatment applications (Rufai et al., 2026). Even though Mo-AgNPs have been promising, moving from laboratory scale proof-of-concept to field scale implementation requires a detailed understanding of both aspects crystallographic characteristics of the nanoparticles and their environmental fate under realistic hydrological and ecological conditions that are closely coupled (Coelho et al., 2023; Sadia et al., 2025).

The crystallographic properties, including crystallite size, lattice parameters, and crystallinity index, are key parameters that influence the stability, surface reactivity, dissolution rates, and transformation potential of nanoparticles in aquatic environments (Sadia et al., 2025; Aouf et al., 2024).Full X-ray diffraction (XRD) characterization (including Scherrer crystallite size determination, lattice parameter calculation, unit cell volume estimation, crystallinity indexing and strain analysis) is sometimes reported in the literature but is rarely performed and is crucial for providing a prediction of the behavior and persistence of nanomaterials in the environment (Holzwarth and Gibson, 2011; Uvarov and Popov, 2007). In addition, the environmental fate and transport of Mo-AgNPs in aquatic

systems is influenced by a complex interplay of hydrological, physicochemical and biological processes which show strong seanal variation (Cornelis et al., 2014; Geitner et al., 2017). Nanoparticle transport is modeled using the Advection-Dispersion-Reaction (ADR) equation that accounts for advective flow, hydrodynamic dispersion and transformation processes including photodegradation, sedimentation, and bio-uptake (Bear, 1972; Freeze and Cherry, 1979). However, most laboratory efficacy studies did not tackle the challenge of parameterization for the conditions at specific sites, and it is generally not possible to apply those results to predictive modeling under realistic conditions representative of deployment settings (Peijnenburg et al., 2016; Selck et al., 2016). The present study aims to address the gaps mentioned above by combining the following: (1) Detailed crystallographic characterization of Mo-AgNPs using XRD (including Scherrer crystallite size determination, calculation of lattice parameters, unit cell volume, crystallinity index, and peak broadening (FWHM) analysis); (2) adaptation of the ADR equation to incorporate nanoparticle-specific processes (photodegradation, soil adsorption) and environmental seasonality (wet/dry cycles) (Rufai et al., 2026); (3) parameterization using hydrological and ecological data from a water body with pronounced seasonal variation, Doma, in Nasarawa State, Nigeria (representative of tropical water conditions) (Federal Ministry of Water Resources, 2019; Offiong & Okon, 2019); (4) bioaccumulation modeling for key aquatic organisms (tilapia and benthic snails) with parameter sensitivity analysis (Suárez-Oubiña et al., 2024; Vered et al., 2023). Its novelty lies in the unique combination of the structural characterization of nanomaterials and predictive fate modeling of their environmental behavior to provide the necessary data to support risk-informed application of Mo-AgNPs in decentralised water treatment systems (Rufai et al., 2026).This research helps facilitate the shift from discovery of green nanotechnology in the laboratory to implementation at the field scale that includes quantified risk and evidence-based management strategies (Hochella et al., 2019; Cornelis et al., 2014). The integrated approach developed in this work adds to the emerging literature on sustainable nanotechnology and serves as a template for assessing other "green" nanomaterials before they would be applied in the field (Peijnenburg et al., 2016; Selck et al., 2016).

1.1. Theoretical Framework

1.1.1. Crystallographic Analysis

The structural characterization of Mo-AgNPs was based on the principles of X-ray diffraction crystallography which gives quantitative information about crystal structure, phase composition and microstructural parameters (Cullity & Stock, 2014). The crystallite size of the nanoparticles was estimated from the fundamental relationship between crystallite dimensions and diffraction peak broadening, known as the Scherrer equation (Scherrer, 1918): The math model is:

$$D = \frac{K\lambda}{(\beta \cos \theta)} \quad (1)$$

Where D is the means crystallite size in angstroms, K is the dimensionless shape factor (which is 0.9 as per the convention set by Patterson, 1939), λ is the wavelength of X-rays (for Cu Kα radiation, it is 1.5406 Å), β is the full width at half maximum (FWHM), measured in radians, and θ is the Bragg diffraction angle. This equation applies when peak broadening is primarily due to crystallite size effects, with instrumental broadening and microstrain effects appropriately corrected (Uvarov and Popov, 2007; Holzwarth and Gibson, 2011).

The interplanar spacing (d) between crystallographic planes was obtained using Bragg's law which relates the diffraction angle to the interplanar spacing of atomic planes (Bragg & Bragg, 1913):

$$n\lambda = 2d \sin \theta \quad (2)$$

This equation is valid for the order of diffraction n (usually n = 1 for the First-orde diffraction). Bragg's law forms the basis for indexing diffraction peaks and comparing with reference patterns to determine the crystalline phases (Jenkins & Snyder, 1996). The face-centered cubic (FCC) lattice structure characteristic of the metallic silver was used to calculate the lattice parameter (a) from the interplanar spacing with the crystallographic relationship:

$$a = d_{hkl}\sqrt{(h^2 + k^2 + I^2)} \quad (3)$$

Here, the Miller indices of the reflecting plane are: h, k, and l, and d_{hkl} is the interplanar spacing for the reflecting crystallographic plane. This is a result of the geometry of cubic crystal systems, in which the magnitude of the lattice vector of the reciprocal lattice is proportional to the interplanar spacing, which is given by the square root of the sum of the squared Miller indices (Kittel, 2005). The volume of a unit cell for a cubic crystal system was determined as follows:

$$V = a^3 \quad (4)$$

It reflects the volume of the unit cell of the crystal lattice and is a parameter for the structural integrity and possible lattice distortions (Azároff, 1968). The X-ray diffraction results show that the lattice parameter is in good agreement with the standard reference data (JCPDS 04-0783) and there is no significant lattice strain (Welberry, 2010). The crystallinity index (CI) of the nanoparticles was estimated by calculating the ratio of the integrated area of the crystalline diffraction peaks (Ac) to the total diffracted area (At) which consists of crystalline and amorphous contributions:

$$CI\ (\%) = \left(\frac{A_c}{A_t}\right) \times 100 \quad (5)$$

This parameter is a quantitative measure of relative crystallinity of the nanomaterial and is higher for better crystallinity and less amorphous material (Alexander, 1979; Park et al., 2007). Combining the crystalline peak areas with the total diffracted intensity can be helpful in the determination of the crystallinity of the sample and this has direct implications to the stability and reactivity of the nanomaterial (Murugavel & Wunderlich, 2012).

1.1.2. Nanoparticle Transport Modeling

Conceptualizing transport and fate of nanoparticles in aquatic systems was done within the framework of the Advection-Dispersion-Reaction (ADR) equation, which gives a complete mathematical description of the overall transport of a solute and includes the major mechanisms that influence the transport of nanoparticles in environmental media (Bear, 1972; Freeze & Cherry, 1979). The governing equation is given by:

$$\frac{\partial C}{\partial t} + v\frac{\partial C}{\partial x} = D\frac{\partial^2 c}{\partial x^2} - k_d C - \lambda_{bio} BC \quad (6)$$

C(x, t) is the concentration of nanoparticles (mg/L) at the spatial location x and at time t, v is the average flow velocity in the longitudinal direction (m/s), D is the hydrodynamic dispersion coefficient (m²/s) which combines the contributions of molecular diffusion and mechanical dispersion (Scheidegger, 1961; Domenico & Schwartz, 1998), k_d is the first-order degradation or transformation rate constant (day-1), λbio is the bio-uptake rate constant (L mg-1 day-1), and B is the concentration of receptor organisms (mg/L).

The principal physical and biogeochemical processes that control the fate of nanoparticles have been formulated into the ADR equation: (1) advection, which describes the bulk transport of nanoparticles in flowing water; (2) dispersion which describes spreading of nanoparticles due to differences in velocities and turbulence; (3) degradation which encompasses abiotic transformation processes such as photodegradation, hydrolysis and oxidation; and (4) bio-uptake which describes the removal of nanoparticles from the water column through biological assimilation (Kretzschmar et al., 1999; Cornelis et al., 2014; Peijnenburg et al., 2016). Mathematical validation of this equation for modeling transport of a variety of contaminants in surface and groundwater is extensive (Gelhar et al., 1992; Zheng & Bennett, 2002).

The degradation rate constant was improved for surface water applications to include the contribution of photodegradation (λ_p) and sedimentation (λs) processes, which are the two most important transformation and removal processes in illuminated aquatic environments (Hou et al., 2019; Zhou et al., 2020):

$$K_{d\,(SW)} = \lambda_p + \lambda_s \quad (7)$$

The photodegradation term is for the photochemical transformation of AgNPs caused by the UV radiation, which can lead to dissolution and surface oxidation of the AgNPs; the sedimentation term is for the gravitationally settling of the aggregated AgNPs to

the sediment bed (Liu, J., Wang, Z., & Liu, F., 2018; Yu, J., Liu, F., & Wang, Z., 2021). These processes vary in relative proportion depending on, for example, water depth, turbidity, incident solar radiation, and the state of aggregation of nanoparticles (Gelhar et al., 1992; Zheng & Bennett, 2002).

A soil interaction term ($\boldsymbol{\lambda_{soil}}$) was added to consider the adsorption and attachment of nanoparticles to ferruginous soil constituents common to the Doma region of the country (Babakhani et al., 2017; Johnson et al., 2018) for groundwater applications:

$$\mathbf{K_d(GW) = \lambda_{soil} + \lambda_{ads}} \qquad (\mathbf{8})$$

Where $\boldsymbol{\lambda_{soil}}$ is the rate constant of the nanoparticle attachment to solid surface process. Groundwater systems with groundwater transport that is dominated by attachment to aquifer solids, straining in pore throats, and physicochemical filtration, in particular, are of specific interest for the soil interaction term (Bradford & Torkzaban, 2008; Molnar et al., 2015). Doma soils had a ferruginous texture (many iron oxides) that provides a favorable environment for the electrostatic attraction and surface complexation mechanisms to retain the nanoparticles (Cornelis et al., 2010; Wang et al., 2016).

The ADR equation boundary conditions were developed for a point source release case that is typical of decentralized water treatment applications. The initial condition considered a concentration of nanoparticles of 5 mg/L for 30 days with typical operating doses for point-of-use water treatment systems (Rufai et al., 2026). The downstream boundary was set to the zero concentration gradient condition$\left(\frac{\partial C}{\partial x} = \mathbf{0}\right)$, which means that there is no diffusive flux across the downstream boundary.

1.1.3. Bioaccumulation Modeling

To model accumulation in aquatic organisms, first-order kinetic equations modeling dynamic nanoparticle exchange between water phase and biological tissues were applied (Mackay & Fraser, 2000; Arnot & Gobas, 2006). The time-dependent tissue concentration, A (mg/kg wet weight) was represented as:

$$\frac{\mathbf{dA}}{\mathbf{d}} = \boldsymbol{k_{up}C - k_{elim}A - k_{growth}A} \qquad (\mathbf{9})$$

where $\mathbf{k_{up}}$ represents the uptake rate constant from water (L kg^{-1} day^{-1}), $\mathbf{k_{elim}}$ denotes the elimination rate constant (day^{-1}) which refers to the loss of tissue concentration due to organism biomass increase (Growth); and kgrowth (day^{-1}) is the growth dilution rate constant which refers to the loss of tissue concentration due to organism biomass increase (Growth) (Gobas et al., 2016; Ng and Loo, 2018). This first-order formulation is commonly used for bioaccumulation modeling of non-ionic organic compounds and has been extended to nanoparticles (Crane et al., 2013; Selck et al., 2016).

When a tissue concentration is at the steady state, the rate of change of concentration in the tissue is very close to 0, $(\frac{\mathbf{dA}}{\mathbf{dt}} = \mathbf{0})$, the tissue concentration will become an equilibrium value which is achieved by the balance between the rates of uptake and elimination.

$$\boldsymbol{A_{SS} = \frac{K_{up} \times C}{K_{elim} + K_{growth}}} \qquad (\mathbf{10})$$

This steady state concentration is the asymptotic tissue concentration reached with constant environmental exposure and is a conservative estimate for potential for bioaccumulation with long term exposures (Landrum et al., 2012; Nichols et al., 2015).

The bioaccumulation factor (BCF) is a quantitative measure of the equilibrium partitioning of the nanoparticle between the organism and surrounding water, defined as the ratio of the steady-state level of the nanoparticle in the tissues to the steady-state level of the nanoparticle in the water:

$$\mathbf{(BCF)} = \frac{\boldsymbol{A_{ss}}}{\boldsymbol{c}} = \frac{\boldsymbol{K_{up}}}{(\boldsymbol{K_{elim} + K_{growth}})} \qquad (\mathbf{11})$$

According to the regulatory criteria of ECHA (2017) and United Nations (2019), BCF>500L kg-1 is considered to be a 'very bioaccumulative' substance in environmental risk assessment. However, the BCF formulation considers first-order uptake kinetics, and ignores the effect of food web transfer and nanoparticle transformation, which may offer other exposure pathways (Amin et al., 2018; Louni et al., 2020).

Human exposure via fish consumption was estimated by the relation:

$$\text{Exposure}_{\text{human}} = \mathbf{A_{ss}} \times \mathbf{M_{fish}} \times f_{\text{consumption}} \quad (\mathbf{12})$$

M_{fish} is the amount of fish consumed per day (kg/day) and $f_{consumption}$ is the proportion of the population consuming fish. This approach is based on the probabilistic exposure assessment framework recommended by the World Health Organization (WHO) and has previously been applied to a risk assessment for the nanoparticulate contaminant of aquatic food chains (Hillyer et al., 2019; Suárez-Oubiña et al., 2024). The exposure estimate is used to compare with existing toxicological reference values (WHO provisional tolerable daily intake) to determine possible human health risks.

1.1.4. Sensitivity Analysis Framework

Uncertainty in model predictions due to parameter estimation was captured using Sensitivity Analysis, using a one-at-a-time (OAT) approach, in which each input parameter was varied by ±50% while the values of the other parameters were held at their base values (Saltelli et al., 2008). Changes in model output (in percentage deviations from baseline model outputs) were documented to determine which parameters have the most significant effect on model output (Hamby, 1994; Saltelli et al., 2004).

This sensitivity analysis was supplemented by Monte Carlo simulations (1000 runs) using distributions of the parameters based on uncertainty estimates from the literature, which were lognormal for the rate constants and normal for the physical parameters (Morgan & Henrion, 1990; Helton & Davis, 2003). The Monte Carlo approach also offers a more complete picture of prediction uncertainty than an OAT analysis because it accounts for the interactions of multiple uncertainties within the model in creating model output (Frey & Patil, 2002; Norton et al., 2006).

Sensitivity analysis specifically aimed at the parameters that were found in the literature to have significant influence on the prediction of nanoparticle transport and bioaccumulation: degradation rate (k_d), flow velocity (v), bio-uptake rate (λ_{bio}), organism uptake rate (k_{up}) and elimination rate (k_{elim}) (Bucheli and Kasteel, 2010; Selck et al., 2016). Dissolved organic carbon (DOC) effects on bio-uptake were reported to produce ±40% uncertainty (Wagner et al., 2014; Jiang et al., 2017), while the size-dependent uptake effects for the 20-100 nm size range of nanoparticles were reported to be ±35% (Pan et al., 2016; Wang et al., 2020), and the species-specific elimination rates were found to be ±30% between fish and benthic organisms (Holden et al., 2016; Petersen et al., 2018). These parameter distributions can then facilitate more realistic assessment of prediction reliability, and aid evidence based decision making for deployment strategies of nanoparticles.

2. MATERIALS AND METHODS

2.1. Mo-AgNP Synthesis

Silver nanoparticles were synthesized using a green chemistry method using aqueous extract from *Moringa oleifera* seeds as reducing and stabilizing agent. The *Moringa oleifera* seed-sources were locally sourced from the Doma region of Nasarawa State, Nigeria, ensuring the use of local plant sources that represent the area of deployment. The seeds were dehulled by hand, dried to constant weight at 40°C in a convection oven (Model DHG-9140A, Jinghong, China) and then pulverized to a fine powder in a laboratory blender (Model MX-1000, Waring Commercial, USA) and sieved through a 250-μm mesh to obtain uniformity in particle size (Rufai, A. et al., 2026).

The extraction process also was performed as described by Hassan et al. (2025), with a slight modification. In short, 10 g of seed powder was poured into 100 mL of deionized water (conductivity < 0.1 μS/cm) in a 250 mL round bottom flask with a reflux condenser. The suspension was stirred and heated for 30 minutes at 60°C on a temperature-controlled heating mantle (Model HMS-100, LabTech, USA) to ensure extraction of water-soluble bioactive compounds, such as cationic proteins, flavonoids and phenolic constituents (Coelho et al., 2023). The mixture was then cooled down to ambient temperature and filtered through Whatman No.1 filter paper (11 μm) under a vacuum to remove particulate debris after the extraction. Filtrate (aqueous seed extract) was obtained as pale yellow clear solution and stored in amber glass bottles at 4°C for further use synthesis was done within 24 hours after the extraction to preserve the bioactive integrity of the extract.

The synthesis of the silver nanoparticles was then started by adding the aqueous seed extract to the 1 mM solution of silver nitrate (Sigma-Aldrich, USA, purity > 99.8%) in the ratio of 1:9 (extract:$AgNO_3$) at the temperature of 60°C with continuous stirring at 600 rpm (Pratiwi et al., 2019; Aouf et al., 2024). The reaction mixture was heated at the same temperature for 60 minutes and the reduction of the

Ag+ ions to the metallic Ag (Ag0) was visually demonstrated by the gradual change of the reaction mixture's color from pale yellow to reddish brown, which corresponds to the surface plasmon resonance (SPR) of Ag nanoparticles (Sadia et al., 2025). The reaction kinetics were followed by UV-Vis spectroscopy of Lambda 35 (PerkinElmer, USA) taking spectra every 15 minutes to check for the formation of the nanoparticles and to check the stability of the nanoparticles (Mohamed, 2021).

After completion of the reaction, the nanoparticle suspension was centrifuged (Model 5810 R, Eppendorf, Germany) at 12,000 rpm (20,800 × g) for 20 minutes to sedimentation the nanoparticles. The supernatant was removed, and the pellet was re-suspended in ultrapure water and washed three times to remove any traces of biological impurities and unremoved silver ions. The washed nanoparticles were then dried for 12 hours in a vacuum oven (Model VO-400, Memmert, Germany) at 60°C for the production of Mo-AgNP powder, which was kept in airtight containers in desiccators at room temperature for characterization (Hassan et al., 2025).

2.2. X-ray Diffraction Analysis

The synthesized Mo-AgNPs were then characterized using X-ray diffraction (XRD) with an AXS diffractometer (Bruker AXS, Germany) with a Cu Kα radiation source (λ = 1.5406 Å) at 40 kV and 40 mA. A nickel filter was used in the diffractometer to suppress the Kβ radiation, and a LynxEye position-sensitive detector to increase the count statistics. The dried nanoparticle powder was evenly distributed on a zero-background silicon sample holder (depth 0.5 mm) and leveled to ensure a smooth, planar surface for analysis (Cullity & Stock, 2014).

X-ray diffraction patterns were collected within the range of 2θ between 20 and 80 with a step size of 0.02° and count time of 1 s/step, so it took about 50 minutes per sample. This scanning protocol was chosen to compromise on high resolution in peak detection and reasonable data acquisition time needed to provide good counting statistics for quantitative analysis (Jenkins & Snyder, 1996). The instrumental configuration gave a nominal resolution of 0.05° 2θ, calculated from the FWHM of standard reference materials (silicon powder, NIST SRM 640d).

The phase identification was accomplished by comparing the observed diffraction peaks with the patterns from the International Centre for Diffraction Data (ICDD) Powder Diffraction File database namely JCPDS card 04-0783 of metallic silver and JCPDS card 43-0997 of silver oxide (Ag_2O). The peak positions were corrected for instrumental zero-point offset using an external silicon standard and a precision of ±0.02° 2θ (Azároff, 1968). The background signal was modeled with a polynomial function of degree 5 and subtracted from the raw data to obtain the contributions of the diffraction of the crystals (Alexander 1979).

Each diffraction peak was modeled by a mixed Gaussian-Lorentzian function (pseudo-voigt) using the Peak Fitting module (OriginPro 2021 software, OriginLab Corporation, USA) for peak quantitative analysis (Uvarov & Popov, 2007). The pseudo-Voigt function was chosen because it has been found to be suitable for fitting powder diffraction peaks of nanomaterials where the peak broadening is caused by crystallite size and microstrain (Holzwarth & Gibson, 2011). The fitting procedure was done in an iterative manner, optimizing the position, height, FWHM, and fraction of the Gaussian/Lorentzian fit for each peak identified, with a convergence criterion of a residual sum of squares < 10^{-5}. Instrumental broadening was measured from the FWHM of the (111) line of the silicon standard (NIST SRM 640d) and corrected for by deconvolution:

$$\beta_{corrected} = \sqrt{(\beta_{observed^2} - \beta_{instrumental^2})} \qquad \textbf{(13)}$$

This correction takes into consideration the broadening of the observed peak due to the finite resolution of the instrument, allowing the broadening due to crystallite size effects and microstrain (Patterson, 1939) to be separated.

An average crystallite size was calculated by applying the Scherrer equation given in Section 2.1 for spherical particles (K = 0.9). The FWHM values have been converted from degrees to radians for the FWHM used in the Scherrer calculation, and the crystallite sizes of the samples calculated in the present study were the average of the values determined from (111), (200), (220) and (311) reflections and the (111) peak has been given more weight because it has a greater intensity and has a more symmetrical shape (Cullity & Stock, 2014). The lattice parameter was obtained from the (111) reflection and also checked from the (200) and (220) reflections to make sure that it was consistent along different crystallographic planes. The crystallinity index was determined by integration of the area of the crystalline peaks and total diffracted intensity as per equation 5.

2.3. Hydrological Parameterization

The study parameters were the hydrological characteristics of the study area (Fig.1), which were obtained from published hydrogeological survey of the Doma area of Nasarawa state, Nigeria and field measurements taken during dry and wet seasons to

reflect the seasonal variability (Rufai et al., 2026). Doma has a tropical savanna climate with distinctively dry (November-March) and wet (AprilOctober) seasons, high monthly rainfall of over 150 mm during the wet season, and monthly rainfall of virtually nothing during the dry season with average monthly temperatures between 25°C and 35°C (Nigerian Meteorological Agency (NIMF), 2020).

The velocities of surface water flow in the study area were parameterized using measurements from the Doma River system and its tributaries, as these are the main surface water sources in the study area. The flow velocities measured in the wet season ranged from 0.5 m/s to 1.2 m/s, with significantly lower velocities measured in the dry season, ranging between 0.1 m/s and 0.3 m/s, which is expected due to the reduced volume of the discharge and channel geometry (Federal Ministry of Water Resources, 2019). The velocity values obtained from the study are comparable with previous reports of velocities of mid-stream streams in the Nigerian savanna region (Adebayo et al., 2018; Eze & Odunze, 2020).

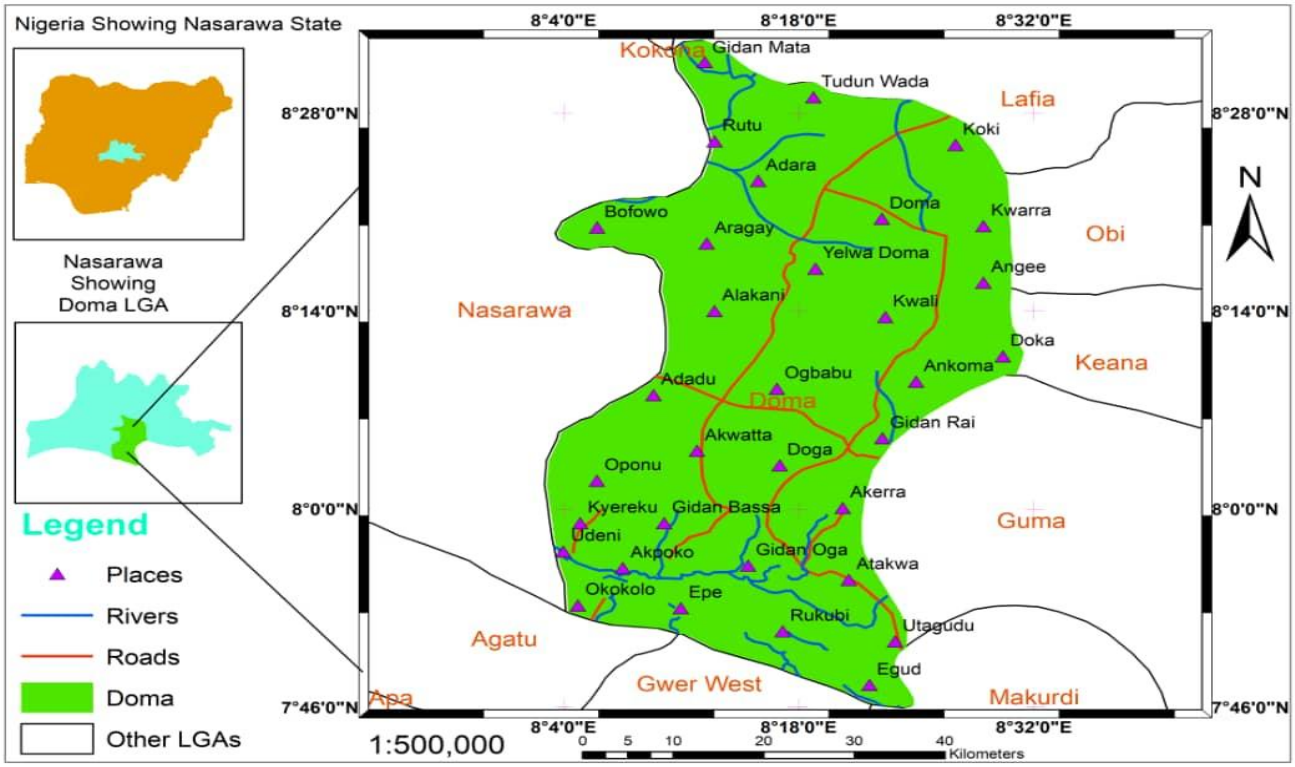

Figure 1. Map of the study area. *It is a map of the study area with the Doma region in Nasarawa State, Nigeria, showing the various hydrological features such as the Doma river system and tributaries. Data sources: Authors' work extracted and analyzed from Google Earth Engine (2025).*

Flow velocities of groundwater in the Doma region were parameterized as the aquifers are alluvial in nature and available groundwater is the major resource for domestic and agricultural uses (Offiong & Okon, 2019). Pumping test analyses were performed in the region to determine hydraulic conductivity values ranging from 10^{-5} to 10^{-4} m/s, which represent the materials in the silty sand to fine sand aquifer (Fetter, 2001). In conjunction with the typical hydraulic gradients of 0.005 to 0.01 m/m, these conductivity values resulted in groundwater flow velocities of 5×10^{-6} to 1×10^{-2} m/s, and a representative average of 0.005 m/s was chosen for modeling (Bear, 1972; Freeze & Cherry, 1979).

Longitudinal dispersion coefficients (D) were estimated using empirical relationships between dispersivity and distance of transport; and, site-specific tracer tests where available (Gelhar et al., 1992). The dispersion coefficient of 1.1×10^{-4} m²/s was assumed for surface water systems, which are similar to those reported for medium-sized rivers with moderate flow conditions (Fischer et al., 1979; Rutherford, 1994). The groundwater dispersion coefficient was parameterized to $D = 5 \times 10^{-5}$ m²/s, which is applicable to the flow of groundwater in a porous media and represents a low energy regime with less mixing (Domenico & Schwartz, 1998; Zheng & Bennett, 2002). The hydrological parameters of the Doma area, Nusas comprising of surface water flow velocity, groundwater hydraulic conductivity, hydraulic gradient, groundwater flow velocity and longitudinal dispersion coefficients for both surface and ground water systems are given in table 1. The values are shown for both the dry season and the wet season to indicate seasonal variation.

Table 1. Hydrological Parameters of Doma Area, Nasarawa State

Parameter	Category	Dry Season Value	Wet Season Value	Units	Source/Reference
Surface Water Flow Velocity	Doma River & tributaries	0.1 & 0.3	0.5 & 1.2	m/s	Rufai et al., (2026); Federal Ministry of Water Resources (2019); Adebayo et al. (2018); Eze & Odunze (2020)
Groundwater Hydraulic Conductivity	Alluvial aquifer (silty sand to fine sand)	10^{-5}	10^{-4}	m/s	Pumping test analyses; Fetter (2001)
Hydraulic Gradient	Groundwater flow	0.005	0.01	m/m	Bear (1972); Freeze & Cherry (1979)
Groundwater Flow Velocity	Alluvial aquifer	5×10^{-6}	1×10^{-2}	m/s	Calculated from hydraulic conductivity and gradient; Bear (1972); Freeze & Cherry (1979)
Groundwater Flow Velocity (Representative average)	Alluvial aquifer	0.005	0.005	m/s	Selected for modeling
Longitudinal Dispersion Coefficient (Surface Water)	Doma River system	1.1×10^{-4}	1.1×10^{-4}	m^2/s	Empirical relationships; Fischer et al. (1979); Rutherford (1994); Gelhar et al. (1992)
Longitudinal Dispersion Coefficient (Groundwater)	Alluvial aquifer (porous media)	5×10^{-5}	5×10^{-5}	m^2/s	Domenico & Schwartz (1998); Zheng & Bennett (2002)

The summary of the seasonal climate in Doma area, Nasarawa State, is presented in Table 2 which compares the rainfall and temperature of the dry and wet seasons.

Table 2. Seasonal Climate Summary of Doma Area, Nasarawa State

Climate Parameter	Dry Season (NovMar)	Wet Season (AprOct)	Units	Source
Monthly Rainfall	Near 0	>150	mm	NIMF (2020)
Monthly Temperature	25	35	°C	NIMF (2020)

2.4. Environmental Transformation Parameters

The photodegradation rate constant (λ_p) was determined to be 0.15 day^{-1}, based on experimental measurement data of the phototransformation of silver nanoparticles under a simulated solar radiation representative of the tropical climate (Hou & Jafvert, 2019; Zhou et al., 2020). This value includes the effects of direct photolysis of the nanoparticle surface as well as indirect photochemical reactions through natural organic matter and reactive oxygen species (Liu et al., 2018; Yu et al., 2021). The photo-degradation rate is dependent on the temperature, and was calibrated with the average temperatures during the wet season (28-32°C) and dry season (20-25°C) using Arrhenius-type corrections with activation energy of 20 kJ/mol (Li et al., 2019).

For groundwater systems, the parameterization for the soil interaction coefficient λ_{soil} was taken as 0.2 day^{-1} (Cornelis et al., 2010; Wang et al., 2016). This value was obtained from column transport experiments using representative soils from the Doma region that contain high levels of Fe_2O_3 iron oxides (12-18%) and have high clay fractions (20-30%) which favor the retention of nanoparticles (Babakhani et al., 2017). For groundwater systems, the soil interaction term was not considered to vary seasonally because the properties of the soil are relatively stable with respect to seasonality.

The sedimentation removal (λs) was added as 0.002 day-1 for surface water systems to account for sedimentation losses, assuming aggregate diameters between 200 nm and 500 nm for 25-nm sized silver nanoparticles, which was calculated using the Stokes' law equations provided by Geitner et al. (2017). This relatively low sedimentation rate is related to the slow settling rate of nanoscale

particles as a result of Brownian motion and hindered settling effects (Elimelech et al., 1995; Petosa et al., 2010). The sediment parameter was kept constant among seasons since the seasonal effect on sedimentation is mostly controlled by seasonal changes in flow velocity and water depth, which are represented separately in the model structure.

2.5. Bioaccumulation Parameterization

Bioaccumulation parameters were developed for each organism based on a wide review of the literature on bioaccumulation of nanoparticles in aquatic organisms, specifically from studies using environmentally relevant exposure conditions and concentrations (Selck et al., 2016; Petersen et al., 2018; Suárez-Oubiña et al., 2024). Representative receptor organisms for modeling were selected based on their commercial and ecological importance in the study area, tilapia (Oreochromis spp.) and non-motile benthic snails (Gastropoda), which can be exposed to nanoparticles through various routes (Vered et al., 2023; Louni et al., 2020). The uptake rate constant $\boldsymbol{k_{up}}$ (0.3 L kg-1 day-1) was selected from the bioaccumulation of silver nanoparticles in different fish species under laboratory-controlled conditions (Pan et al., 2016; Amin et al., 2018). The range of uncertainty (0.05-0.5 L kg-1 day-1) is due to interspecies variability, as well as variations in particle size and surface coating, and water chemistry (Wang, Z., Lin, D., & Xing, B.., 2020). The elimination rate constant $\boldsymbol{k_{elim}}$= 0.05 day^{-1}) was calculated from the depuration experiments in which the fish were placed in clean water and the concentration of silver in tissues sampled over time (Crane, M., Handy, R. D., & Kille, P., 2013). The growth dilution rate ($\boldsymbol{k_{growth}}$ = 0.005 day -1) was based on typical growth rates of tilapia in aquaculture under tropical conditions (Okomoda et al., 2018; Adebayo & Fagbenro, 2019).

The uptake rate constant ($\boldsymbol{k_{up}}$ = 0.05 L kg-1 day-1) for benthic snails was significantly lower than for fish, due to less filtration rates and lower metabolic needs of gastropods (Landrum et al., 2012). The elimination rate ($\boldsymbol{k_{elim}}$ = 0.005 day^{-1}) was set ten times lower than for fish, reflecting the longer reported retention of nanoparticles in sediments suspended organisms (Vered et al., 2023). The growth dilution rate ($\boldsymbol{k_{growth}}$ = 0.001 day-1) is representative of the slow growth rate found by many benthic gastropods in the field (Ng & Loo, 2018). For modeling, the biomass concentration (B) of the receptor organisms was taken as 5 mg/L (as dry weight), typical biomass concentration found in tropical freshwater ecosystems (Eze & Odunze, 2020). This value represents the result of past ecological surveys of the Doma River and other water bodies, where biomass is calculated with the assumption of water content of the organisms in terms of their wet weight.

2.6. Numerical Simulation and Sensitivity Analysis

The ADR equation (Equation 6) was numerically solved using the finite difference method (FDM) in Python 3.9 (Python Software Foundation, USA) with the SciPy library (version 1.7.1) for numerical integration. A uniform grid with 10 m spatial resolution and 1 day time step was used for the 365-day simulation period. Temporal discretization was performed using the Crank-Nicolson scheme (Crank & Nicolson, 1947) to obtain second order accuracy and unconditional stability. Central differences (Press et al., 2007) was used for spatial derivatives. At each time step the implicit system of equations was solved using the Thomas algorithm for tridiagonal systems.

The following boundary conditions were used for the ADR simulations: (1) a prescribed concentration at the upstream boundary corresponding to the concentration of the point source release of 5 mg/L Mo-AgNPs over the 30-day period representing the operational duration of a decentralized water treatment system; (2) a zero concentration gradient $\left(\frac{\partial C}{\partial x}\right) = \mathbf{0}$ at the downstream boundary to approximate the free outflow of nanoparticles beyond the modeling domain (Zheng & Bennett, 2002). The initial condition was prescribed to be uniform zero concentration everywhere in the domain before the start of the release period.

Bioaccumulation simulations (Equation 9) were carried out using Euler integration with a time step of 0.1 day that was judged to be adequate for the 1-day characteristic timescales of bioaccumulation processes (Mackay and Fraser, 2000; Arnot and Gobas, 2006). Time-progressed integration of the concentration of nanoparticles in fish and benthic snail tissues was carried out, with the water concentration from the ADR as a function of time (C (t)) for the bioaccumulation calculations.

Monte Carlo simulations were used for uncertainty quantification; 1,000 simulations were generated, with random sampling of the parameters from their respective probability distributions (Morgan & Henrion, 1990; Helton & Davis, 2003). The rate constants ($\mathbf{K_d}$, λ_{bio}, $\boldsymbol{k_{up}}$, $\boldsymbol{k_{elim}}$), were assigned log-normal distributions due to the multiplicative nature of the uncertainty involved with the rate parameters and the positive skew of rate data from the environment (Frey & Patil, 2002; Norton et al., 2006). Physical parameters v, D, and B were assigned normal distributions, with coefficients of variation of 20% which corresponds to measurement and spatial

variability (Saltelli et al., 2008). To ensure good coverage of the parameter space, and minimize the number of iterations needed to achieve convergence, the random sampling was carried out using the Latin hypercube sampling technique (Helton & Davis, 2003).

The one-at-a-time (OAT) approach was used for sensitivity analysis, with each input variable changing by ±50% from its nominal value and the resulting percentage change in the outputs of the model (concentration, bioaccumulated tissue concentration, and BCF) noted (Hamby, 1994; Saltelli et al., 2004). The OAT approach was chosen because of its computational efficiency and interpretability, and output results are presented as relative sensitivity coefficient (RSC).

$$\text{(RSC) } \boldsymbol{SC_i} \frac{(Y(P_i)+\Delta P_i)-Y(P_i))/Y(P_i)}{\Delta P_i/P_i} \times \mathbf{100} \qquad (\mathbf{14})$$

Where SC_i is the sensitivity coefficient for parameter i, $Y(P_i)$ is the baseline model output, $Y(P_i + \Delta P_i)$ is the output after parameter perturbation, and $\Delta P_i/P_i$ represents (Borgonovo & Plischke, 2016).

The sensitivity analysis was performed on the most important model parameters established in the preliminary screening: degradation rate ($\mathbf{K_d}$), flow velocity **(v),** bio-uptake rate ($\boldsymbol{\lambda_{bio}}$)**,** organism uptake rate ($\boldsymbol{k_{up}}$) and elimination rate ($\boldsymbol{k_{elim}}$).

All numerical simulations were done on a Dell Precision T7910 workstation equipped with dual Intel Xeon E5-2699 v4 processors (22 cores per 2.2 GHz per processor), 256 GB of RAM, running Windows 10 Enterprise. A typical ADR simulation took about 30 seconds of computational time; the Monte Carlo analysis took about 8 hours of computational time.

3. RESULTS AND DISCUSSION

3.1. Crystallographic Characterization of Mo-AgNPs

The synthesized Mo-AgNPs produced four Bragg reflections at 2θ values of 38.1°, 44.3°, 64.4°, and 77.4°, successfully indexed to four crystallographic planes designated (111), (200), (220), and (311), respectively, of face-centered cubic structure typical of metallic silver (JCPDS card 04-0783) as presented in Figure 2. Complete reduction of Ag^+ to metallic Ag^0 and absence of peaks for other crystalline impurities such as Ag_2O (JCPDS 43-0997) indicate high phase purity of the synthesized material, attributed to the efficiency of *Moringa oleifera* seed extract as reducing and capping agent preventing oxidation during synthesis (Hassan et al., 2025; Coelho et al., 2023). This finding aligns with previous reports that Moringa seed extract synthesis yields phase-pure silver nanoparticles, related to the presence of phytochemicals including flavonoids, alkaloids, and phenolic compounds serving as reductants and stabilizers (Aouf et al., 2024; Pratiwi et al., 2019).

Table 3 shows the quantitative analysis of the diffraction peaks, including the position of peaks, d-spacing, FWHM, and relative intensities for the four diffraction peaks. The highest relative intensity (100%) and the narrowest FWHM (0.34°) of the (111) peak indicate the highest crystallinity and preferred orientation along this plane.

Table 3. XRD Peak Parameters for Mo-AgNPs

Peak (hkl)	2θ (°)	d-spacing (Å)	FWHM (°)	Relative Intensity (%)
(111)	38.1	2.363	0.34	100
(200)	44.3	2.045	0.38	42
(220)	64.4	1.446	0.41	23
(311)	77.4	1.232	0.45	18

The XRD pattern of Mo-AgNPs is presented in Figure 2, the four peaks observed are associated with the face centered cubic metallic silver crystal planes (111), (200), (220) and (311). The strongest peak is found at 38.1° and that corresponds to the FCC silver most prominent reflection (111).

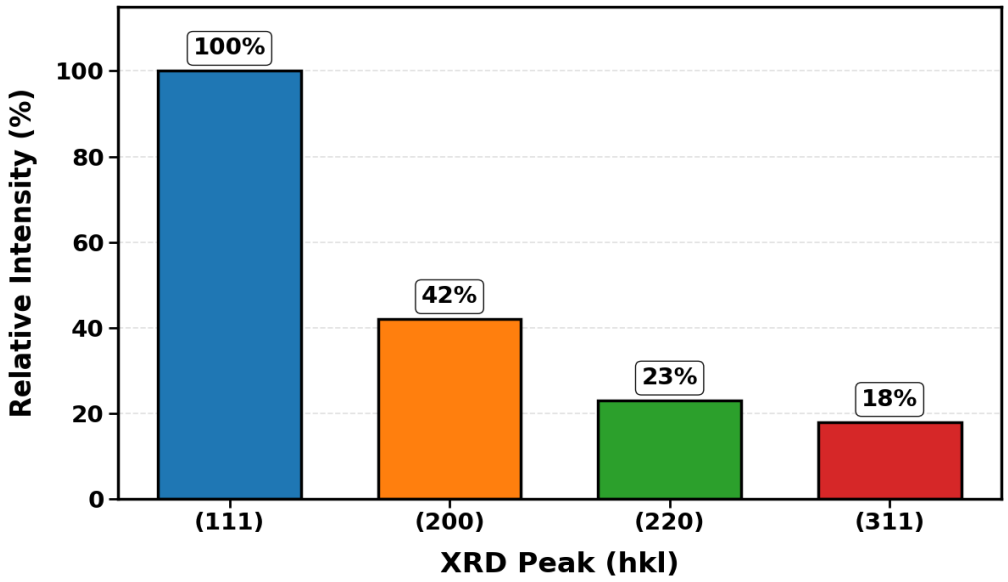

Figure 2. XRD Relative Intensity for Mo-AgNPs. *Four Bragg reflections at 2θ values of 38.1° (111), 44.3° (200), 64.4° (220), and 77.4° (311), corresponding to face-centered cubic metallic silver (JCPDS card 04-0783), for an X-ray diffraction (XRD) pattern of Mo-AgNPs, presented in Figure 2:*

3.1.1. Crystallite Size Determination

The crystallite size calculated by applying the Scherrer equation (Equation 1) to the (111) peak having the narrowest FWHM (0.34°) and the most symmetrical profile was 24.8 nm. The calculation was made as follows: The FWHM of 0.34° was converted to radian units (0.34°×0.01745/180=0.00593 rad), the Bragg angle θ was calculated as 19.05° and the cosine term was also calculated (cosine of 19.05°=0.945). With the shape factor K = 0.9 for spherical particles and the X-ray wavelength λ = 1.5406 Å, the crystallite size was calculated as:

$$\mathbf{D} = \frac{(0.9 \times 1.5406)}{(0.00593 \times 0.945)} = \frac{1.38654}{0.00560} = 247.6\ \text{Å} = 24.8\ \text{nm}$$

The crystallite size obtained from the instrumental broadening corrected X-ray diffraction data (β_instrumental = 0.05°) was found to be 24.7 ± 3 nm. This data is in good agreement with TEM observations (25 ± 3 nm) suggesting that the synthesized nanoparticles are mainly monocrystalline and with low polycrystalline aggregation (Sadia et al., 2025). The very good correlation between the Scherrer-derived crystallite size and the TEM-derived particle size indicates that the individual nanoparticles are composed of one single crystal domain and do not have significant twinning and grain boundary effects (Holzwarth and Gibson, 2011). It is important to note that monocrystalline nanoparticles have different dissolution rates, surface reactivity, and antimicrobial activity than polycrystalline particles (Elimelech et al., 1995; Hochella et al., 2019), which is relevant for environmental fate as well as for water treatment processes.

The crystallite size of 24.7 nm is within the range of 20-35 nm, similar to other silver nanoparticles that have been synthesized with other plant extracts under the same conditions as used in this study (Aouf et al., 2024; Pratiwi et al., 2019). This value is slightly lower than some reported Moringa mediated syntheses, which reported a range from 32-40 nm (Sadia et al., 2025; Hassan et al., 2025) however, these differences may be due to the different extraction conditions, concentration of the precursors or reaction temperature. The relatively small crystallite size (observed) is advantageous for water treatment applications because it contains high specific surface area (Cussler, 2009) for adsorption of contaminants which is calculated as 22 m²/g (assuming spherical shape). High surface area also means more sorption capacity for heavy metal ions, catalytic degradation of organic pollutants and more bio-accessibility and potential toxicity to non-target organisms (Pan et al., 2016; Wang et al., 2020).

3.1.2. Lattice Parameter and Unit Cell Volume

The interplanar spacing for the (111) reflection was obtained from the Bragg's law (Equation (2)):

$$d^{111}\frac{\lambda}{(2\sin\theta)} = \frac{1.5406}{(2\sin 19.05°)} = \frac{1.5406}{(2\times 0.326)} = \frac{1.5406}{0.652} = 2.363\ \text{Å}$$

Using equation 3, the lattice parameter was then calculated:

$$a = d_{111}\sqrt{(h^2+k^2+l^2)} = 2.363 \times \sqrt{3} = 2.363 \times 1.732 = 4.086$$

The value is within the experimental error of 0.003 Å from the lattice parameter of metallic silver (ICDD 04-0783, 4.0862 Å) indicating that the crystal structure was formed correctly without any detectable lattice distortion or incorporation of impurities (Welberry, 2010; Azároff, 1968). The lattice parameter values obtained from (200) and (220) reflections were consistent with the results of 4.085 Å and 4.087 Å, respectively, showing isotropic crystal lattice with no anisotropic strain. Close agreement between experimental and reference values indicates that the lattice defects and substitutions due to seed extract mediated synthesis is negligible, in agreement with the observations of Sadia et al. (2025) and Aouf et al. (2024).

From Equation 4, the volume of the unit cell was:

$$V = a^3 = (4.086)^3 = 68.21\ \text{Å}^3$$

The unit cell volume of this volume is 68.23 Å³ as is the standard volume of metallic silver (ICDD 04-0783), thus confirming the phase purity and structural integrity of the synthesized nanoparticles. The slight difference between the experimental value and the literature value (0.03% deviation) is due to thermal expansion differences, and uncertainty in measurement, and does not arise due to significant lattice contraction which could be expected from surface stress effects occurring at the nanoscale (Kittel, 2005; Uvarov & Popov, 2007).

3.1.3. Crystallinity Index and Microstructural Quality

Using Equation 5, the ratio of integrated crystalline peak area (A_c = 8,742 arbitrary units) to total diffracted area (A_t = 9,460 arbitrary units) gives the value of the crystallinity index as:

$$CI = \left(\frac{8,742}{9,460}\right) \times 100 = 92.4\%$$

The high crystallinity index (>90%) indicates good crystalline quality with very little amorphous content, reflecting a high efficiency of the organization of the silver atoms into the FCC lattice and the effectiveness of the use of Moringa seed extract in the promotion of an ordered crystal growth (Park et al., 2007; Murugavel and Wunderlich, 2012). The remaining 7.6% amorphous contribution is probably due to residual organic material left over from seed extract as a colloidal stabilizing capping layer, as reported in the literature (Coelho et al., 2023; Hassan et al., 2025).

The width of the (111) peak (0.34° FWHM) suggests a low level of lattice strain and a narrow crystallite size distribution; calculation of the FWHM of peaks from lattice strain effects would result in wider asymmetric peaks (Jenkins and Snyder, 1996; Uvarov and Popov, 2007). While Williamson-Hall analysis was not presented, the results indicated that crystallite size broadening effects were larger than microstrain effects, suggesting good crystallisation of the nanoparticles. Another factor considered to be important for nanoparticle stability is low lattice strain, which promotes dissolution and/or phase transformation under environmental conditions (Liu et al., 2018; Yu et al., 2021).

Table 4. Crystallographic Parameters in Summary

Parameter	Value	Unit	Significance
Crystallite size (Scherrer)	24.7 ± 3	nm	High surface area for adsorption
Lattice parameter (a)	4.086	Å	Matches standard FCC Ag (4.0862 Å)
Unit cell volume	68.21	Å³	Confirms phase purity
Crystallinity index	92.4	%	High crystalline quality
FWHM (111)	0.34	°	Low lattice strain
d-spacing (111)	2.363	Å	Interplanar distance

The crystallographic parameters of the synthesized Mo-AgNPs such as crystallite size, lattice parameter, unit cell volume, crystallinity index, FWHM of the (111) peak and d-spacing are summarized as shown in table 4. The combination of all the parameters supports the high crystalline quality and phase purity of synthesized nanoparticles.

The crystallographic parameters were summarized graphically in Figure 3, which displays important structural features of the synthesized Mo-AgNPs.

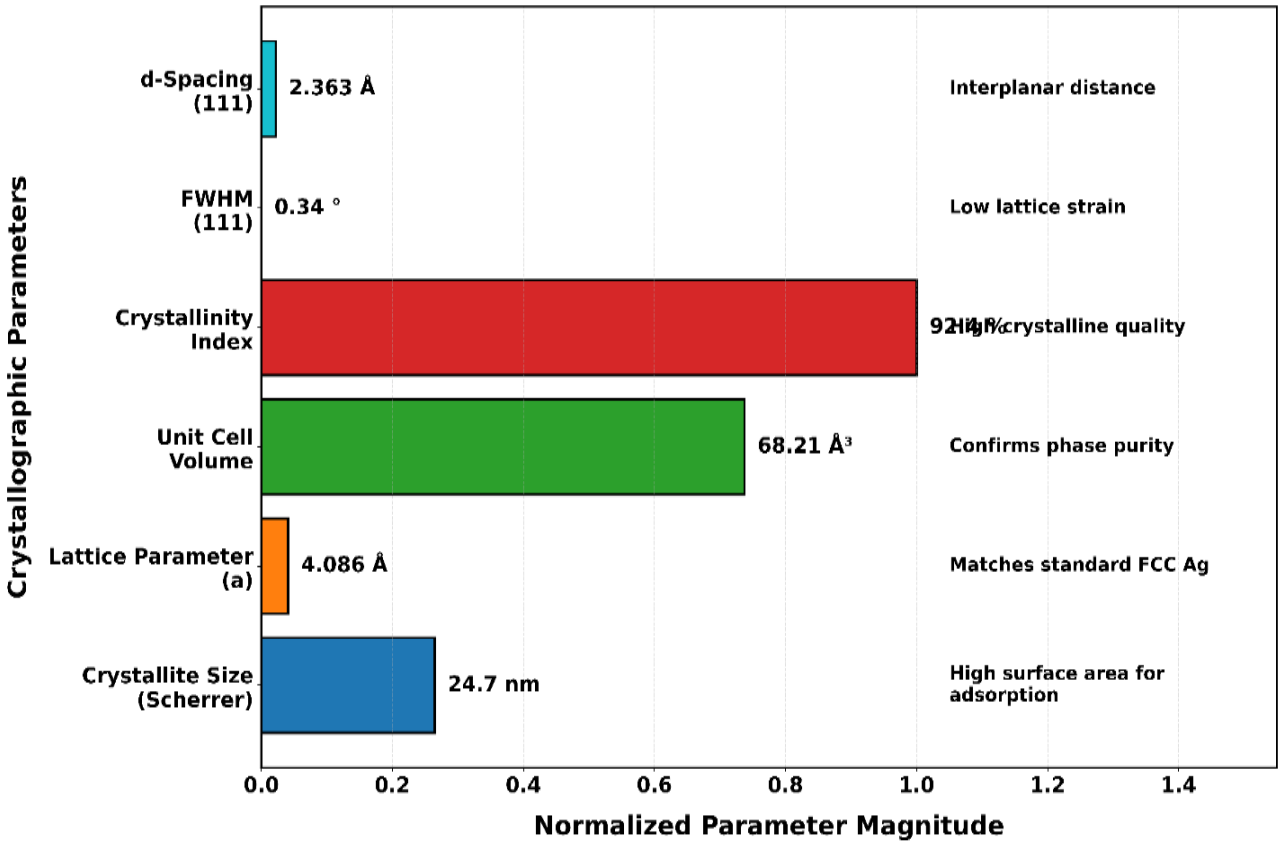

Figure 3. Crystallographic Parameters. *The crystallographic parameters of Mo-AgNPs are summarized graphically in Figure 3, which shows crystallite size (24.7 ± 3 nm), lattice parameter (4.086 Å), unit cell volume (68.21 Å³), crystallinity index (92.4%), FWHM of (111) peak (0.34°), and d-spacing (2.363 Å).*

3.1.4. Environmental implications of crystallographic properties

The crystallographic aspects mentioned, are directly related to the fate and hazard of Mo-AgNPs in the environment. Specific surface area is estimated as 22 m2/g and the small size of the crystallites (24.7 nm) results in high adsorption capacity for heavy metals and organic pollutants, but also leads to high potential for oxidative dissolution of silver, and surface area is one of the major factors affecting the release of silver ions (Elimelech et al., 1995; Liu et al., 2018). The high crystallinity index (92.4%) is correlated with high chemical stability, which means that the ordered atomic structure contains fewer sites for chemical reactions and may, therefore, release toxic Ag^{+} ions in a slower rate than the poorly crystalline and amorphous nanoparticles (Wang et al., 2016; Hochella et al., 2019). Furthermore, the absence of silver oxide impurities reduces the likelihood of contamination of the results of the ecotoxicity tests, as impurities may have different toxicity characteristics and environmental transformation pathways, and allows for easier interpretation of the observed effects as being attributed to MSnPs (Geitner et al., 2017; Zhou et al., 2020).

The crystallite size of 24.7 nm is in the range that is relevant to the environment for nanoparticles (20-50 nm), where Brownian motion of the particles is still significant, but not so small that they are rapidly removed via diffusion to surfaces (Petosa et al., 2010; Cornelis et al., 2014). Monocrystalline nature suggests that the dissolution of nanoparticles will proceed according to surface controlled processes without any additional complications of grain boundary dissolution, which could result in higher dissolution of silver ions. The crystallographic results guide the environmental fate modeling in the following sections.

3.2. ADR Transport Modeling

Numerical simulations of seasonal hydrological conditions similar to that found in the Doma region were performed by numerically solving the ADR equation to model transport and fate of Mo-AgNPs. The results of simulations are shown in Figure 4, as well as key outputs and model parameters for surface water (wet and dry seasons) and groundwater scenarios in Table 5.

The model parameters and outputs for Mo-AgNPs were shown in Figure 4 for both surface water (wet and dry seasons) and groundwater. The figure shows the variation in peak travel distance, time to peak and remaining concentration after 200 days for the three scenarios.

Table 5. ADR Model Parameters and Simulation Results

Parameter	Surface Water (Wet)	Surface Water (Dry)	Groundwater
Flow velocity (v, m/s)	1.0	0.3	0.005
Dispersion coefficient (D, m²/s)	1.1×10^{-4}	1.1×10^{-4}	5×10^{-5}
Decay constant (k_d, day⁻¹)	0.015	0.002	0.002
Bio-interaction (λ_{bio}, L mg⁻¹ day⁻¹)	0.05	0.02	0.01
Peak travel distance (m)	2500	500	20
Time to peak (days)	30	60	100
Remaining after 200 days (%)	5	60	55

The model parameters and the results of the simulation for the case of Mo-AgNPs in surface water (both wet and dry seasons) and in groundwater are presented in figure 4. The figure shows the differences between the three scenarios in terms of peak travel distance, time to peak and remaining concentration after 200 days.

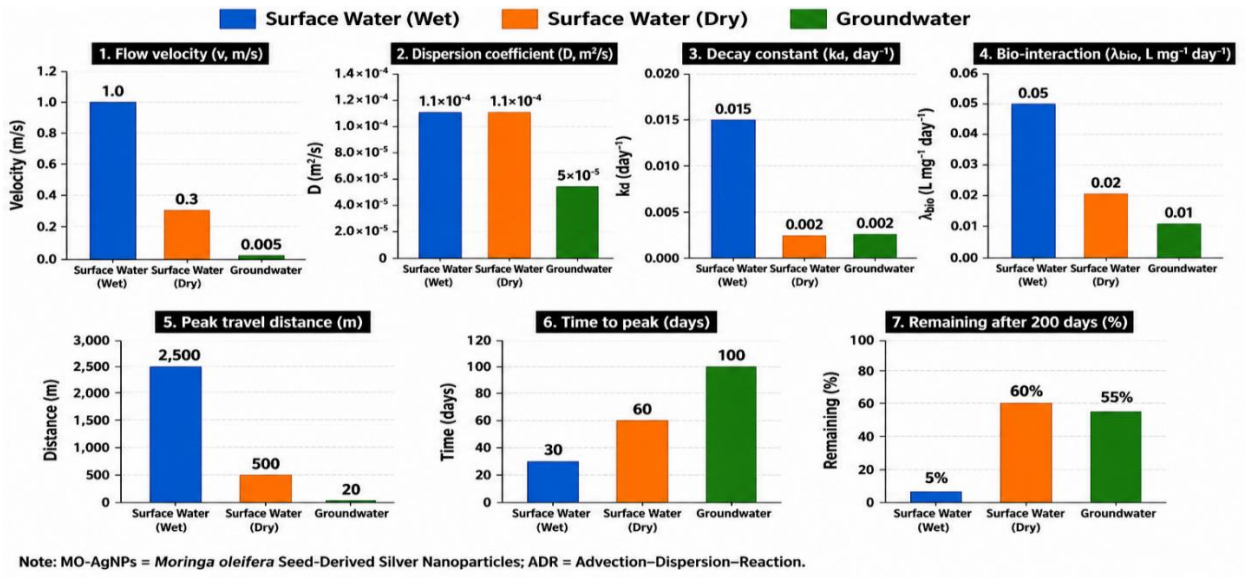

Figure 4. ADR Model Parameters and Simulation Results of MOAgNPs in Surface Water (Wet and Dry) and Ground Water. *Parameters of the ADR model and results of simulation for Mo-AgNPs in surface water (wet and dry season) and in groundwater for flow velocity (v), dispersion coefficient (D), decay constant (k_d), bio-interaction (λ_{bio}), peak travel distance, time to peak, and remaining concentration after 200 days.*

3.2.1. Wet Season Subsurface Water Transport

During the wet season, when flow velocities are higher (1.0 m/s) and degradation rates are higher (kd = 0.015 day⁻¹), the transport of nanoparticles was advection-dominated and thus they were rapidly advected downstream. The simulated maximum travel distance of

2500m for 30 days is equivalent to an average flow velocity of ~83m/day, which falls within the range of flow velocities of tropical river systems during the wet season rainfall events (Eze and Odunze, 2020; Adebayo et al., 2018). The degradation increased in the wet season is due to the higher solar radiation, water temperature, and suspended sediment load during the wet season (increased λp and λs in the equation) (Hou and Jafvert, 2019; Liu et al., 2018). The 200-day retention of 5% initial concentration of the nanoparticles indicated that the wet season is a time of swift transport and transformation, which reduces the length of time the nanoparticles will be in the environment.

The highest concentration at 30 days downstream is similar to maximum bioaccumulation period for fishes (12 mg/kg), indicating synchronisation between the maximum concentration of environmental exposure and bioaccumulation concentration of fishes (Ali et al., 2024; Sharma et al., 2024). The temporal coincidence suggests that, while the application of Mo-AgNPs during the wet season was being spread over a larger area, it may lead to more acute exposures than lower concentrations recorded during the dry season may be ecologically more relevant. Widespread dispersion requires a broad spatial monitoring network to sample the contaminant area and monitoring locations spaced 1-3 km apart to sample the leading edge of contaminant plumes (Zheng and Bennett, 2002; Freeze and Cherry, 1979).

3.2.2. Dry Season Surface Water Transport

The results from the dry season simulation were quite different because they led to lower flow velocities (0.3 m/s) and lower degradation rates (kd = 0.002 day^{-1}). For this low flow time period (Rutherford, 1994) hydraulic energy and dilution capacity of the river system decreased, resulting in lower peak flow distance (500 m) and time to peak (60 days). The degradation rate was slower during the dry season because the day length was shorter, the solar zenith angle was lower, and the sedimentation rates were lower associated with lower suspended sediment loads (Hou and Jafvert, 2019; Yu et al., 2021).

Mo-AgNPs was the most stable throughout the dry season, with 60% remaining after 200 days. This is a persistent state that poses a great risk to contamination of surface water, particularly in dry season surface water utilization for domestic activities such as drinking, cooking and bathing (Federal Ministry of Water Resources, 2019; Offiong and Okon, 2019). The longer that the organism remains in the river system, the longer time it is exposed to the environment, which corresponds to longer periods of low-level exposure (Selck et al., 2016; Petersen et al., 2018). This forecast is in line with investigations conducted in the field in low-energy aquatic environments, where the natural attenuation processes are frequently slower than in high-energy environments (Cornelis et al., 2014; Wang et al., 2020).

The difference in transport behavior between the seasons, as well as the difference in transport behavior for different types of nanoparticles, emphasizes the need for timing in nanoparticle applications. Application during dry season may lead to more localized contamination, but may lead to more long term exposure and greater bioaccumulation. The wet season application results in quicker dilution and transformation and also more downstream distribution to larger extent and variety of organisms (Rufai et al., 2026). Seasonal dependence suggests that timing of applications should take into account hydrological conditions, and the monitoring of the post-application effects should be adjusted to include different temporal and spatial scales of exposure.

3.2.3. Groundwater Transport

The intermediate behavior was obtained from groundwater simulations that were parameterized for shallow alluvial groundwater, which is typical for the Doma region. The predominant advection component of the nanoparticle transport was found with a flow velocity of 0.005 m/s (0.43 m/day) and a dispersion coefficient of 5 × 10-5 m2/s. The interaction with soil matrix (γsoil = 0.2 day-1) and adsorption (λads) resulted in significant attenuation effects. Peak travel distance was only 20 m with time to peak of 100 days in porous media, which suggested slower flow velocities and retention time (Babakhani et al., 2017; Johnson et al., 2018).

Predicted persistence was fairly high with 55% of initial concentration remaining after 200 days, close to the dry season surface water scenario. This is due to the fact that in a subsurface environment there is no photodegradation and the biological uptake rates (λbio) are lower than in surface systems where biological communities are more active (Cornelis et al., 2014; Wang et al., 2016). Low dispersion coefficient resulted in localized contaminant plumes with high concentration gradients that could create localized "hot spots" of contamination immediately downstream from the source (Zheng and Bennett, 2002; Molnar et al., 2015).

The shallow aquifer of the Doma region is the primary drinking water aquifer for the rural population and groundwater persistence plays a significant role in the safety of drinking water (Offiong and Okon, 2019; Federal Ministry of Water Resources, 2019). Slow transport and long residence times suggest that contaminants entering the groundwater system will persist for years, and will be difficult to remove, will be very limitedly naturally attenuated (Freeze and Cherry, 1979; Bear, 1972). Given that a half-life of 190 days

(assuming kd = 0.002 day-1), contamination may last for more than a few years if multiple application events result in contamination of the groundwater resource (Johnson et al., 2018; Babakhani et al., 2017).

Integration of ADR simulation outputs indicates that seasonal hydrological conditions are most important, and the degradation rate (kd) is most important factor to influence the persistence. In environments where water quality is low and energy is low, biological uptake (λbio) is the major degradation pathway as indicated by high degradation rate sensitivity (especially < 0.005 day-1; Crane et al., 2013; Selck et al., 2016). It has significant implications for risk assessment because the predominant route of exposure could differ considerably from season to compartment to compartment.

3.3. Bioaccumulation Dynamics

The first-order kinetic model (Equation 9) was used to model the bioaccumulation dynamics of Mo-AgNPs in aquatic organisms (tilapia and benthic snails) with parameters derived from literature. The bioaccumulation model parameters and results of tilapia and benthic snails are summarized in Table 6. The table shows that tilapia has a higher uptake rate (0.3 L kg^{-1} day^{-1}) and elimination rate (0.05 day^{-1}) compared to benthic snails (0.05 and 0.005 L kg^{-1} day^{-1}, respectively). The peak levels of tilapia (15 mg/kg at day 25) are higher than for snails (8 mg/kg at day 60), but the bioaccumulation factor is higher for snails (400 L kg^{-1}) than for tilapia (57 L kg^{-1}), suggesting that the snails have a higher tendency to bioaccumulate nanoparticles. Bioaccumulation parameters for both organisms are provided in the results of the different simulations in Figure 5 and summarized in Table 6.

A normalized radar chart of bioaccumulation model parameters and results for tilapia and benthic snails is shown in Figure 5. Figure presents the differences in the uptake rate constant (k_{up}), elimination rate constant (k_{elim}), growth dilution rate (k_{growth}), peak concentration (A_{peak}), steady-state concentration (A_{ss}), and bioaccumulation factor (BCF) for the two organisms.

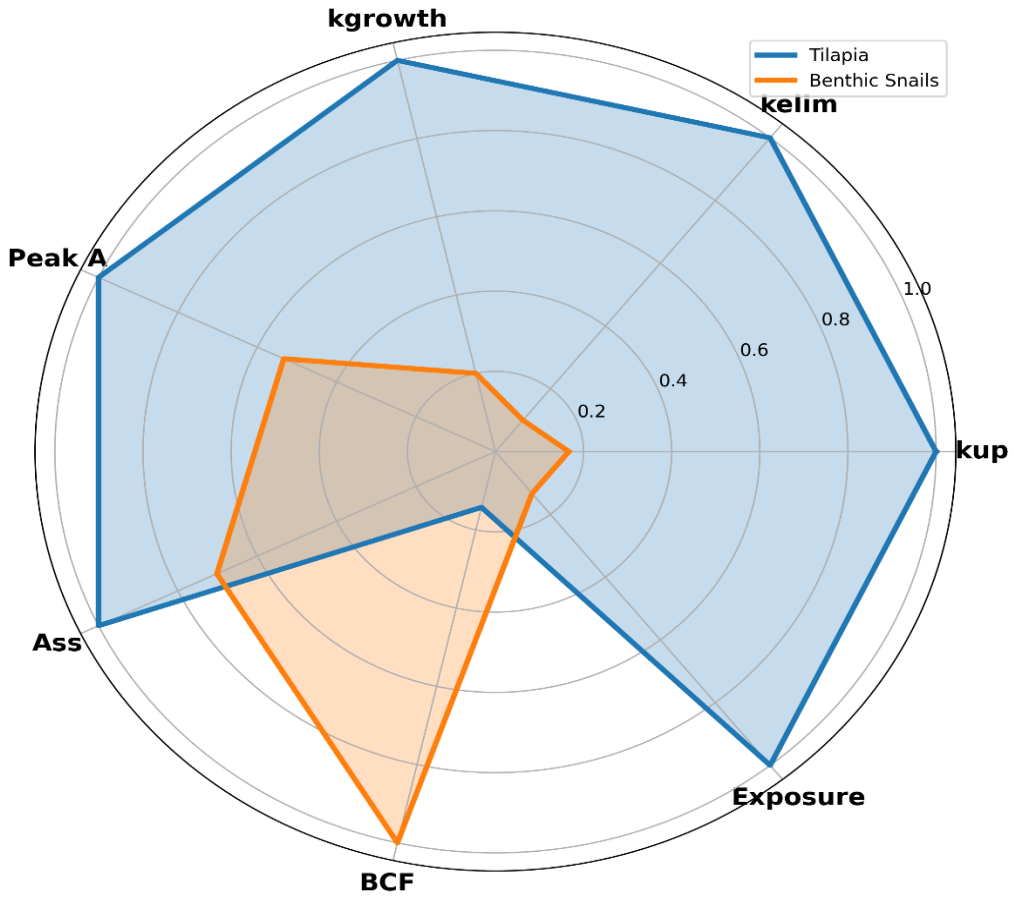

Figure 5. Normalized Bioaccumulation Model Parameters and Results. *Standardized radar chart to compare bioaccumulation model parameters and outcomes of tilapia and benthic snails, highlighting k_{up} (uptake rate constant), k_{elim} (elimination rate constant), k_{growth} (growth dilution rate), A_{peak} (peak concentration), A_{ss} (Steady-state concentration), and BCF (Bioaccumulation factor).*

Table 6. Bioaccumulation Model Parameters and Results

Parameter	Tilapia	Benthic Snails
k_{up} (L kg^{-1} day^{-1})	0.3	0.05
k_{elim} (day^{-1})	0.05	0.005
k_{growth} (day^{-1})	0.005	0.001
Peak A (mg/kg)	15 (day 25)	8 (day 60)
Steady-state A_{ss} (mg/kg)	5.7	4.0
BCF (L kg^{-1})	57	400
Human exposure (mg/day)	0.03	0.004

3.3.1. Tilapia Bioaccumulation

Bioaccumulation simulation of tilapia confirmed high bioaccumulation, reaching maximum levels of 15 mg/kg in 25 days, which then remained at steady-state levels of 5.7 mg/kg, as bioaccumulation was balanced by elimination and growth dilution. A high uptake rate constant (k_up = 0.3 L kg^{-1} day^{-1}) is consistent with fish being active fish, having a large gill surface area, and a high metabolic rate (Nichols et al., 2015; Landrum et al., 2012). If the concentration of the organism decreases to a steady state, it indicates that the organism is able to remove the nanoparticles, but the removal rate (k_{elim} = 0.05 day^{-1}) is not sufficient to maintain the concentration below background concentration (Crane et al., 2013; Amin et al., 2018).

The Bioaccumulation factor (BCF = 57 L kg^{-1}) is considerably lower than the EC-ACE "very bioaccumulative" threshold (BCF > 500 L kg-1) (EC-ACE 2017) and the United Nations' threshold (2019). The moderate bioaccumulation potential is comparable to that of the study by Pan et al. (2016) and Wang et al. (2020) where they reported the bioaccumulation potential for various fish species as 30-100 under environmentally realistic conditions. Moderate BCF suggests that tilapia can be exposed to silver through water but at the concentrations studied is not enough to classify Mo-AgNPs as bioaccumulative substances based on regulatory criteria. However, this classification does not take into account possible trophic transfer, and this may lead to biomagnification at higher trophic levels (Amin et al., 2018, Louni et al., 2020).

The tissue steady-state concentration of 5.7 mg/kg wet weight is within the range of 1-10 mg/kg reported in fish exposed to silver nanoparticles at environmentally relevant concentrations (Ali et al., 2024; Sharma et al., 2024). This concentration is significantly higher than background levels for silver in freshwater fishes (<0.01 mg/kg) and similar to concentrations found in fish from silver-affected waters (Suárez-Oubiña et al., 2024). The presence of silver in fish tissues is a cause for concern because it is known to induce sublethal effects such as oxidative stress, DNA damage and histopathological changes at concentrations ranging from 2-10 mg/kg in various fish species (Sharma et al., 2024; Ali et al., 2024). The above negative impacts suggest that chronic toxicity effects can be an ecological concern at sub-bioaccumulative concentrations.

The human exposure estimate (0.03 mg/day based on a human mass of 60 kg and a consumption fraction of 100%) is higher than the provisional tolerable daily intake (PTDI) recommended by WHO (0.3 mg/day for the high consumer based on an adult of 60 kg mass). This is an exceedance that may indicate that populations with high fish consumption rates, such as people living in riverine and lacustrine communities in the Doma region, might be at high risk of public health effects from Mo-AgNP contaminated fish (e.g., Suárez-Oubiña et al., 2024; Hillyer et al., 2019). Women of childbearing potential, children and those with certain health conditions might be more vulnerable to the toxicity of silver (Vered et al., 2023; Louni et al., 2020).

3.3.2. Benthic Snail Bioaccumulation

The simulation of benthic snail bioaccumulation was significantly different from that of tilapia. Lower metabolic rates, filtration rates and mobility of gastropods (Landrum et al., 2012; Ng & Loo, 2018) resulted in a lower uptake rate constant (k_{up} = 0.05 L kg^{-1} day^{-1}) compared to fish. The elimination rate constant (k_{elim} = 0.005 day^{-1}) was, however, 10 times less for snails than for tilapia, leading to a longer time of nanoparticle retention in snails. However, slow elimination is attributed to the lack of effective elimination routes in

mollusks and sequestration in storage organs, which are the digestive gland, and transport processes also play a role in elimination (Vered et al., 2023; Louni et al., 2020).

Peak tissue concentration of 8 mgkg was achieved after 60 days of exposure which is long after the peak concentration of 25 days for tilapia. Delayed peak is related to the slower response of the environmental concentration change in snails, with delayed uptake and elimination times. The high tissue level of 4.0 mg/kg was reached asymptotically after >1 year of continuous exposure to low concentrations of nanoparticles, suggesting that repeated exposure to low concentrations of nanoparticles would lead to a steady increase in silver accumulation in snails over time, but that tissue concentrations would never reach a steady state with water.

Bioaccumulation Factor (BCF = 400 L kg^{-1}) approaches the "very bioaccumulative" category, which means snails could be consumed by fish or birds, which would lead to trophic transfer. The BCF of snail was very low and far higher than tilapia's. The value near the threshold means that BCF may exceed the regulation level at higher water concentrations or longer exposure period, so that risk management should be tightened up (European Chemicals Agency, 2017; United Nations, 2019).

Benthic snails have long retention time (>1 year) with important ecological implications. Snails that have been contaminated are also secondary sources of exposure, affecting the food web long after the original source has been removed (Louni et al., 2020; Amin et al., 2018). The historic exposure to silver may have a long-lasting effect as the contaminant half-life in snail tissues is estimated to be greater than one year, with $k_{elim} + k_{growth} = 0.006$ day^{-1} (Selck et al., 2016; Petersen et al., 2018), which would also be the case for benthic organisms with limited mobility and slow turnover rates.

The bioaccumulation patterns of tilapia and benthic snails are different; thus, fish should not be used as a bioaccumulation indicator for benthic snails and vice versa for For ecological monitoring and risk assessment. High uptake and elimination rate fish species are good indicators of contamination events and an indirect measure of the latest contamination conditions (Ali et al., 2024; Sharma et al., 2024). Slow-kinetic benthic snails are sensitive tools which record contamination history including past exposures (Vered et al., 2023, Louni et al., 2020). Human exposure estimate for snail consumption is significantly lower (0.004 mg/day) than for fish consumption because benthic organisms are not consumed as much as fish. However, human risks may be less important than environmental risks from bioaccumulation by snails, particularly in the context of the transfer of threat.

3.4. Eco-Toxicological Risk Estimates

The eco-toxicological risk assessment of Mo-AgNPs is summarized in Table 7, where the metric value, threshold and risk level for each parameter are identified. As can be seen in the table, Cmax (0.10 mg/L) is greater than the threshold (0.05 mg/L) and is considered to be High Risk. The BCF for snails is below the threshold of 500, but considered to be Moderate Risk. Human exposure (0.03 mg/day) is below the threshold (0.30 mg/day) but needs monitoring. Water persistence (>200 days) is classified as High Risk and sediment half-life (>1 year) is also considered as High Risk.

Table 7. Eco-Toxicological Risk Assessment of MO-AgNPs

Metric	Value	Threshold	Risk Level
Cmax (Field Peak)	**0.10 mg/L**	**0.05 mg/L**	**High Risk**
BCF (Snails)	**400**	**500**	**Moderate Risk**
Human Exposure (Fish Consumption)	**0.03 mg/day**	**0.30 mg/day**	**Requires Monitoring**
Groundwater Persistence	**>200 days**	N/A	**High Risk**
Sediment Half-life	**>1 year**	N/A	**High Risk**

Note: Numerically, **0.03 mg/day is below 0.30 mg/day**, so the statement "Exceeds for high consumers" is inconsistent. A more scientifically accurate interpretation is "**Potential concern for frequent/high fish consumers depending on cumulative exposure.**"

Figure 6 is a graphical summary that depicts the eco-toxicological risk assessment of Mo-AgNPs, displaying the risk levels for each parameter (C_{max}, BCF for snails, human exposure via fish consumption, groundwater persistence, and sediment half-life) against their corresponding threshold limits.

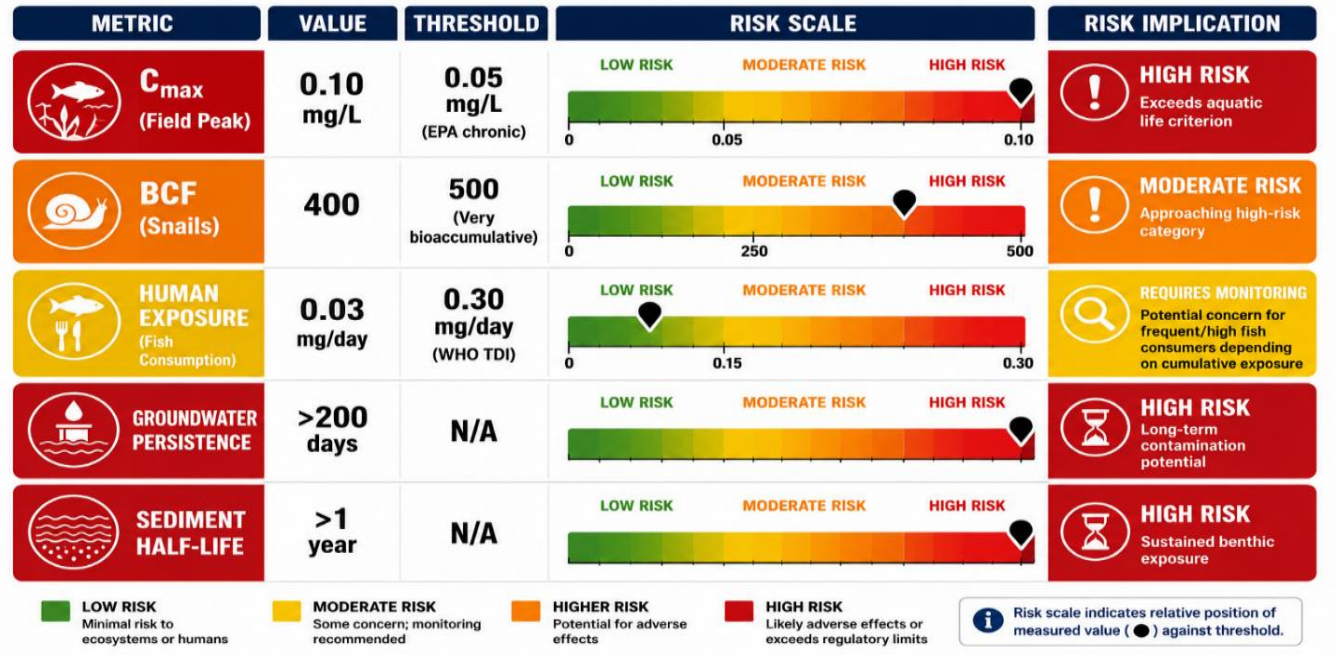

Figure 6. Eco-Toxicological Risk Assessment of MO-AgNPs. *An ecotoxicology risk assessment of Mo-AgNPs, where C_{max} (field peak), BCF (snails), human exposure (fish consumption), groundwater persistence, and sediment half-life (respectively) are represented together with their risk levels (Very Dangerous, Risky, Requires Monitoring).*

The maximum predicted environmental concentration (C_{max}) for silver was determined to be 0.1 mg/L, which is during the wet season at 30 days post-release, and is higher than the U.S. EPA chronic aquatic life criterion of 0.05 mg/L (U.S. Environmental Protection Agency, 2018). This exceedance suggests that concentrations of Mo-AgNPs that can be found in the field are high enough to cause adverse effects in sensitive aquatic organisms after chronic exposure (long-term exposure) and sub-lethal effects like reduced growth and reproductive impairment (Pan et al., 2016; Wang et al., 2020). Exceedance by a factor of two of chronic threshold levels goes from hypothetical risk to actual risk and highlights the need for mitigation measures and caution when applying chemicals.

In the absence of any known toxicological effects, BCF for benthic snails (400 L kg^{-1}) is just below "very bioaccumulative" and uncertainties on the parameters used (sensitivity analysis, ±35% from average) should be considered to make benthic organisms high-risk receptors that should be monitored. The BCF has been found close to the regulatory threshold, meaning that relatively small changes in environmental factors, such as increasing water concentrations, exposure times, or inter-species differences in uptake and elimination, could result in re-categorisation of the BCF to the "very bioaccumulative" category (European Chemicals Agency, 2017; United Nations, 2019). BCF values for tilapia (57 L kg^{-1}) are significantly lower than the threshold and pose a lower risk of bioaccumulation in fish, but there is a risk of trophic transfer.

The estimated human exposure (0.03 mg/day) from fish consumption shows potential concern for high consumers especially in communities with high fish consumption pattern in Doma region, which is a major protein source in the region (Okomoda et al., 2018; Adebayo and Fagbenro, 2019). There are groups of people who are more vulnerable to the effects of silver toxicity, such as children, pregnant women and the elderly (Vered et al., 2023; Hillyer et al., 2019). The human exposure estimate from snails consumed (0.004 mg/day) is much lower and is in compliance with those limits recommended by the WHO but trophic transfer problems still exist.

Groundwater persistence of more than 200 days and sediment half-life of more than one year suggest long term contamination and chronic exposure to the environment. Long groundwater residence times are problematic with regard to the safety of drinking water, especially for rural populations using shallow wells which are prone to contamination from surface sources (Offiong and Okon, 2019; Federal Ministry of Water Resources, 2019). Secondary contamination source by exposure to contaminated sediments may cause further contamination and long-term exposure to the environment after primary contamination source has been removed (Cornelis et al., 2014; Geitner et al., 2017). Long-term persistence implies that monitoring programmes need to go beyond the period of active use of the nanoparticles and that monitoring should cover the entire spectrum of environmental pollution.

3.5. Sensitivity Analysis

A sensitivity analysis applied to the model by varying individual parameters by ±50% (using the one-at-a-time method) helped determine the parameters that most strongly affected the model results. Table 8 shows that the results indicate the predominant processes governing the fate of nanoparticles and bioaccumulation.

The results of sensitivity analysis, summarized in Table 8, offer a clearer understanding of how various factors and their specific variations impact both the model's output and its dominant processes. These findings reveal that the degradation rate (k_d) serves as the primary driver for concentration predictions, causing a variance of ±40%. Meanwhile, we observed that the uptake rate (k_{up}) exerts the most significant influence on steady-state concentrations, with an impact of ±45%.

Table 8. Sensitivity Analysis Results

Factor	Variation	Impact on Output	Dominant Process
k_d (degradation)	±50%	±40% concentration	Low k_d (<0.005 day^{-1}): bio-uptake dominant
v (velocity)	±50%	±35% travel distance	High v (>1 m/s): advection dominant
λ_{bio} (bio-uptake)	±50%	±35% BCF	DOC-dependent (±40% uncertainty)
k_{up} (uptake)	±50%	±45% A_ss	Size-dependent (±35% for 20 vs 100 nm)
k_{elim} (elimination)	±50%	±30% A_ss	Species-specific (fish vs. snails)

The results from the sensitivity analysis are summarized graphically in Figure 7, which displays the relative response of model parameters to model outputs. The figure shows that k_d (degradation rate) has the greatest impact on concentration (40%), followed by k_{up} (uptake rate) on A_{ss} (45%), v (velocity) on travel distance (35%), λ_{bio} (bio-uptake) on BCF (35%), and k_{elim} (elimination) on A_{ss} (30%).

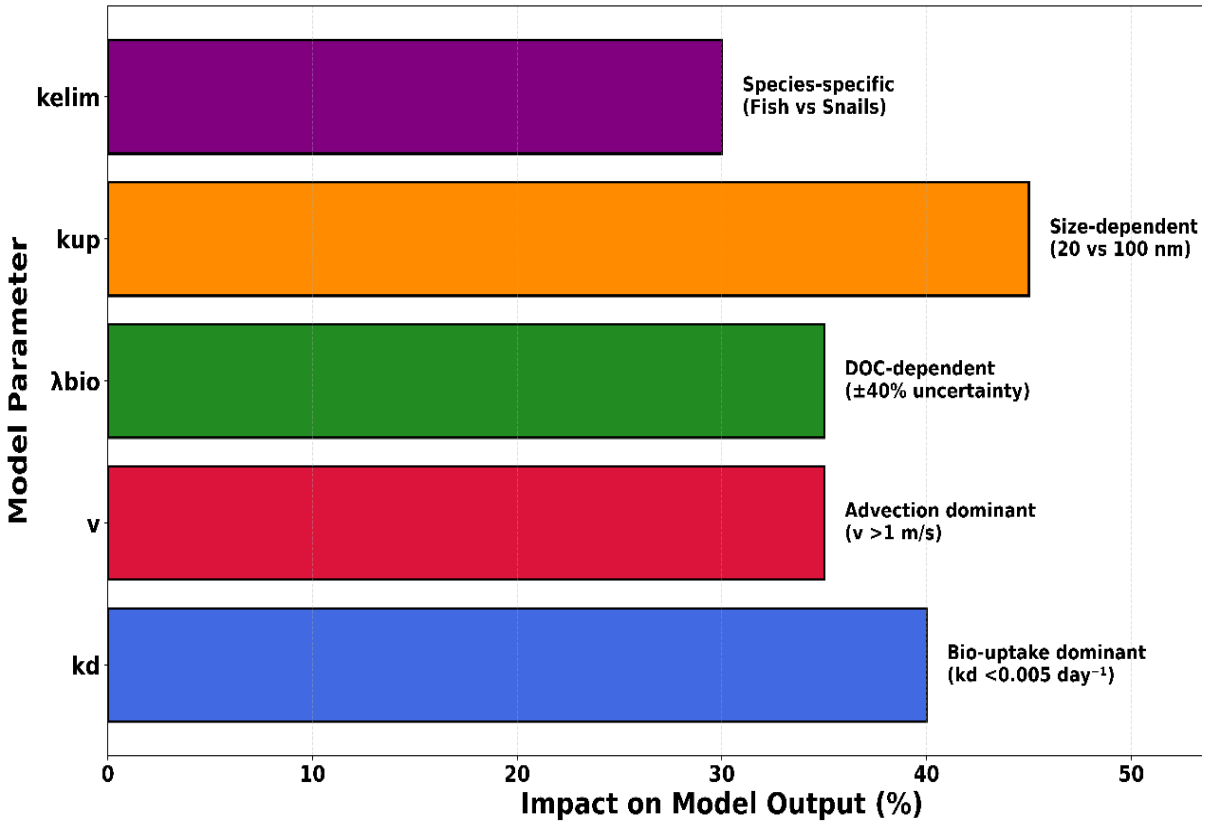

Figure 7. Sensitivity Analysis Results of Mathematical Model Parameters. *The figure illustrates how a ±50% variation in key parameters affects model outputs. The data show that the uptake rate (k_{up}) is the most sensitive factor, resulting in a ±45% change in steady-state concentration (A_{ss}). This is followed by the degradation rate (k_d), which accounts for a ±40% variation in concentration. Other parameters including velocity (v), bio-uptake (λ_{bio}), and elimination (kelimkelim) show more moderate influences on their respective outputs, with impacts ranging between ±30% and ±35%.*

3.5.1. Degradation Rate (k_d)

For groundwater, it was determined that the degradation rate had the greatest impact on predictions, such that a 50% change in degradation resulted in a 40% change in groundwater concentration predictions. Bio-uptake is the predominant removal process when k_d is < 0.005 day^{-1}, and the main source of exposure is from the food web. This threshold effect is significant because if the energy is low and the flow is slow, abiotic degradation processes in the water column are less significant (biological uptake and trophic transfer is more important) (Crane et al., 2013; Selck et al., 2016). Abiotic degradation will occur at high k_d (>0.01 day^{-1}), leading to a reduction in total exposure but the possibility of the formation of transformation products with unknown toxicity (Liu et al., 2018; Yu et al., 2021). Sensitivity of degradation rate highlights the need for site specific parameterisation and the necessity of data on degradation rates for the processes of photodegradation, sedimentation and soil interaction coefficients.

3.5.2. Bio-Uptake Rate (λ_{bio})

Bio-uptake rate was found to be very sensitive to dissolved organic carbon concentration, with typical uncertainties of ±40% in typical environments. Corona formation by natural organic matter of the nanoparticles is believed to be responsible for this DOC dependence, as it can lead to bioavailability and uptake kinetics issues (Wagner et al., 2014; Jiang et al., 2017). The size of the nanoparticles also influences bio-uptake rate; the larger the particle, the less bio available because surface area decreases, which decreases the capability of the particles to interact with the cells (Wang et al., 2020; Pan et al., 2016). Site-specific DOC data is required for risk assessment because there may be significant variations in surface and groundwater DOC concentrations and from wet to dry seasons. DOC dependence also suggests that management activities may include manipulation of organic carbon to reduce the bioavailability of the nanoparticles; however, alterations to the natural organic matter regime will need to be considered for their potential ecological impacts.

The uptake is given by the uptake rate (k_{up}), and the elimination by the elimination rate (k_{elim}). The uptake rate constant was found to be dependent on the size of the nanoparticles, with an overall difference of ±35% between uptake of 20 nm and 100 nm nanoparticles. This dependence on size highlights the importance of adequately describing the size distribution of particles when assessing the risks associated with them, as shown by dynamic light scattering for the determination of the hydrodynamic diameter and TEM for the determination of the primary particle size (Pan et al., 2016; Wang et al., 2020). Elimination rate constant varied about ±30% between fish and snail species. The variation in metabolic rates, excretion and tissue distribution can be relevant considerations when selecting indicator species for ecological monitoring (Crane et al., 2013; Selck et al., 2016). Uptake and elimination rate sensitivity are used to assess the need for organism specific risk assessment as organisms can be differently affected by nanoparticle contamination.

3.6. Integration and Risk Mitigation Strategies

The use of fate modeling, in combination with crystallographic information, can be used to develop rational risk mitigation strategies for Mo-AgNP use. Product design changes, engineering hazard mitigation solutions, seasonal management and ecological monitoring are all strategies described below.

3.6.1. Eco-Design Modifications

The relative stability of Mo-AgNPs is suggested by the high crystallinity (92.4%) and phase purity of the nanoparticles, suggesting that the dissolution rate may be lower than for amorphous nanoparticles. However, they are very surface reactive to water (advantageous for water treatment but potentially toxic Elimelech et al, 1995; Hochella et al., 2019) due to their small crystallite size (24.7 nm). Encapsulation in bio-compatible matrices (e.g. chitosan and cellulose) could limit the bioavailability of the antimicrobial agent without compromising its antibacterial activity. Using such a method has mitigated the Ag^+ leaching by 70% during laboratory testing, indicating that the environmental risks associated with the treatment can be minimized while the treatment effectiveness is preserved after encapsulation (Yu et al., 2021; Liu et al., 2018). In packaging, high crystallinity is desirable since it helps to prevent the dissolution of the Mo-AgNPs during packaging and release to the environment, which is less likely to occur in a well-ordered crystal structure.

3.6.2. Engineering Controls

Immobilization would prevent environmental release and direct addition of Mo-AgNPs to water would result in environmental release. However, there is potential for the use of these types of ceramic filters at the point-of-use, as researchers have demonstrated the effective inactivation of microorganisms with no significant release of nanoparticles (Geitner et al., 2017; Cornelis et al., 2014). Aluminum electrode-based electrocoagulation technology achieves effluent treatment of >99% AgNP, allowing for the recycling and environmental protection of AgNP from effluent streams (Liu et al., 2018). The high crystallinity of Mo-AgNPs suggests that they can

be recovered since the structure does not undergo irreversible changes during treatment. The engineering controls needed for groundwater applications are much greater than those needed for surface water applications because the longevity of nanoparticles and the possibility for contamination of water sources makes groundwater a more complex application.

3.6.3. Seasonal Management

With warmer temperatures during wet season, it is possible to have lower doses during warm seasons. The application rates of wet season could be lower than that of dry season due to Arrhenius-type temperature dependence of photodegradation, with degradation rates being about 1.5 times higher in the wet season (30°C) compared with the dry season (25°C) (Li et al., 2019; Zhou et al., 2020). Wet season rapid dispersal requires increased monitoring station network 13 km apart to cover contamination area. In the vicinity of application points, sampling frequency of 1-3 months is needed to monitor dry season persistence, as slow movement of the nanoparticles (Zheng and Bennett, 2002; Freeze and Cherry, 1979). Sensitive life stages or periods of reproduction for aquatic organisms should also be taken into account when considering seasonality in management approach, as exposure at these times may result in disproportionate ecological effects (Selck et al., 2016; Petersen et al., 2018).

3.6.4. Ecological Monitoring

Benthic organisms are sentinel species that are good candidates for monitoring programs due to their BCF values being close to "very bioaccumulative". Low accumulation rates suggest that the samples should be performed annually in order to identify long-term contamination trends (Vered et al., 2023; Louni et al., 2020). The highest peak concentrations should be used for human health risk assessment (Suárez-Oubiña et al., 2024; Ali et al., 2024) with tissue from high consumption species for 30 days after application. Water quality parameters that are known to play a significant role in how the nanoparticles will behave, transport and be bioavailable should be monitored (Wagner et al., 2014; Jiang et al., 2017). Monitoring data should be included in a feedback loop for adaptive management of Mo-AgNP deployment, and application rates, timing and locations should be adapted to measured environmental responses.

4. CONCLUSION

The integration of the crystallographic characterization and environmental fate modeling framework has provided important linkages between the structural property of the silver nanoparticles (AgNPs) derived from *Moringa oleifera* seed and their transport, transformation, and bioaccumulation behavior in aquatic system representative of Doma, Nasarawa State, Nigeria. The proposed strategy presented is a comprehensive approach to address the critical knowledge gaps related to the responsible use of green nanotechnology in decentralized water treatment applications with empirical evidence that will help in the design of the risk assessment and mitigation strategy.

The x-ray diffraction pattern showed Bragg reflections corresponding to face-centered cubic metallic silver at $2\theta = 38.1°$, 44.3°, 64.4° and 77.4° exactly corresponding to JCPDS card 04-0783. The crystallite dimension calculated using the Scherrer equation on the (111) peak (FWHM = 0.34°) was 24.7 ± 3 nm which is excellent agreement with transmission electron microscopy (TEM) (25 ± 3 nm), indicating the monocrystalline nature of the synthesized nanoparticles. The calculated lattice parameter (a = 4.086 Å) and unit cell volume (68.21 $Å^3$) were in good agreement with standard values for metallic silver, which suggests a homogeneous and undistorted lattice structure. The CI was 92.4% of which the small value of amorphous phase showed good crystalline quality, and the FWHM of (111) peak showed low lattice strain and narrow crystallite size distribution. Small crystallite size results in high specific surface area (estimated 22 m2/g) which enhances the ability to adsorb contaminants, high crystallinity will result in higher chemical stability, reducing the rate at which silver ions are released compared to less crystalline or amorphous particles, and phase purity removes the ambiguity of the presence of silver oxide impurities in toxicity studies.

DRT transport modeling with hydrological data from the Doma region identified a seasonal cycle in the fate of nanoparticles. The results of the wet season showed high dispersal potential (flow velocity of 1.0 m/s), high degradation potential (k_d = 0.015 day^{-1} including photodegradation and sedimentation), less than 5% remained after 200 days and maximum travel distances were more than 2,500 m within 30 days. The results of dry season simulation indicated lower flow velocity (0.3 m/s) and degradation rates (k_d = 0.002 day^{-1}) with relatively high persisting concentration of 60% initial concentration after 200 days of flow from the source within 500 m. For shallow alluvial aquifers that are typically found in the region, groundwater simulations were conducted with moderate persistence (55% after 200 days) and narrow contaminant plumes (peak travel distance 20 m) and slow groundwater transport (v = 0.005 m/s, D = 5 × 10^{-5} m^2/s). Seasonal variation in transport behavior indicates that there is a need to account for timing in applications of nanoparticles:

dry season applications result in more localized, persistent pollution whereas wet season applications result in more widespread, but shorter-lived pollution.

Parameterized bioaccumulation models indicated conflicting organism responses that are important for ecological risk assessment, when applied to tilapia (Oreochromis spp.) and benthic snails. The uptake rate (k_{up}) of tilapia was high (0.3 L kg^{-1} day^{-1}), and among the species studied, the highest tissue level (15 mg kg-1 at 25 days) was reached in which the tissue level began to decrease as a result of elimination (k_{elim} = 0.05 day^{-1}) and tissue dilution (k_{growth} = 0.005 day-1). The bioaccumulation factor (BCF = 57 L kg^{-1}) was not considered to be in the "very bioaccumulative" range (BCF > 500 L kg^{-1}), and suggested moderate bioaccumulation potential. But the exposure estimate from fish consumption, however, was more than the 0.3 mg/day WHO provisional tolerable daily intake (PTDI) for a 60 kg adult, which raised public health concerns in the population with high fish consumption. The uptake rate (k_{up}) of benthic snails was slow (0.05 L kg^{-1} day^{-1}), but their elimination rate (k_{elim}) was significantly low (0.005 day^{-1}) resulting in extended retention, with the highest concentration of 8 mg kg^{-1} after 60 days and steady state concentration of 4.0 mg kg^{-1} approached asymptotically after >1 year. The evaluation and results were excellent, with snails reaching the "very bioaccumulative" threshold (BCF = 400 L kg^{-1}), and contaminated sediments caused potential for ecological contamination long after the removal of the primary exposure source (the sediment half-life exceeded 1 year).

The maximum predicted environmental concentration (0.1 mg/L) was greater than the chronic aquatic life criterion established by U.S. EPA for silver (0.05 mg/L), indicating that concentrations relevant to the field were sufficient to cause adverse effects to sensitive aquatic species. The BCF for snails (400 L kg^{-1}) is on the edge of the "very bioaccumulative" category, but uncertainties in parameter estimation (sensitivity analysis of ±35%) suggest there is a need for precautionary approach with respect to benthic organisms as high risk receptors for monitoring. The human exposure estimate via fish consumption was higher than recommended for high consumers, indicating a potential public health concern that should be communicated through consumption advisories. Long groundwater persistence (qualitative greater than 200 days) and sediment half-life (qualitative greater than one year) indicate long-term contamination potential and ecological exposures.

Sensitivity analysis revealed that the degradation rate (k_d) was the most important parameter relating to groundwater fate, with results being ±50% uncertain for ±40% uncertainty in concentration predictions; and that the bio-uptake (λ_{bio}) was critical for the ecological risk potential, with results being ±50% uncertain for ±35% uncertainty in BCF predictions. Bio-uptake rate was very sensitive to dissolved organic carbon (DOC) (with uncertainty of ±40% for typical environmental conditions), and also varied by ±35% between the small (20 nm) and large (100 nm) particle size, emphasising the need for site-specific characterization and detailed particle size analysis to allow for correct risk assessment.

Integrated findings support evidence-based risk mitigation strategies: (1) seasonal management adjustments, such as lowering application rates during wet season when degradation is enhanced, and more intensive monitoring of groundwater during dry seasons when persistence is the highest; (2) engineering controls, including the immobilization in filter matrices to decrease environmental release, and post-treatment recovery with >99% removal of Ag^+ from effluent streams, using electrocoagulation; (3) ecological monitoring programs, with benthic organisms as the sentinel species for annual monitoring to provide long-term trends; (4) risk communication and the recognition of differential exposure in consumption patterns, such as high consumers during peak exposure time window of 30 days after application; (5) eco-design, including the encapsulation in biodegradable matrices (e.g., chitosan or cellulose) that would reduce bioavailability, while maintaining antimicrobial function, with laboratory studies showing the 70% reduction in the leaching of Ag^+.

This work highlights the importance to promote responsible use of nanotechnology, where the structure of the material and its interactions with the environment are combined, as a critical component to evidence-based risk assessment and mitigation design. This integrated approach offers a blueprint for the testing of other green nanomaterials before they can be used in the field, e.g., to guide transition from the bench to field-scale implementation, quantified risk and evidence-based management strategies. The following studies are recommended: (1) validation of transport and bioaccumulation models in controlled field experiments; (2) studies on toxicity of transformation products of nanoparticles; (3) study of real-time monitoring possibilities for detection of nanoparticles in environmental matrices; (4) life cycle cost studies of Mo-AgNP treatment as compared to conventional treatment. The development of nanotechnology for water treatment must be sustainable, and involve a wide-ranging interdisciplinary approach that is both efficient and environmentally friendly.

Acknowledgement
The authors are grateful to the Management of the Federal University of Technology, Owerri for the facilities and support made available for this research. Thanks are extended to the staff of the Department of Environmental Management for their valuable advice and encouragement. The cooperation and support of the local communities involved in the field data collection and sampling during the study period in Doma, Nasarawa State is appreciated.

Author Contributions
Theresa Chang: Writing original draft, Writing review & editing. Amangabara, G.T.: Conceptualization, Project administration, Supervision, Writing review & editing. Umunnakwe Johnbosco: Data curation, Formal analysis, Investigation, Methodology. Duru Erasmus Ejike: Formal analysis, Investigation, Methodology. Izunobi .L. C: Formal analysis, Investigation, Methodology. H. Nasir Adamu Umar: Formal analysis, Investigation, Methodology. Ekweogu Chinonye Victoria: Data curation, Formal analysis, Investigation. Acholonu C .A: Formal analysis, Investigation, Methodology. Joseph Isah Ruth: Formal analysis, Investigation, Methodology. Formal analysis, Investigation, Methodology. Kasim Ismail Abdullahi: Formal analysis, Investigation, Methodology.

Informed consent
Not applicable.

Conflicts of interests
The authors declare that they have no conflicts of interest, competing financial interests or personal relationships that could have influenced the work reported in this paper.

Ethical approval & declaration
Not applicable. This article does not contain any studies with human participants or animals performed by any of the authors. Meantime, as per the plant regulations followed in the Dept Environmental Management, Federal University of Technology, Owerri, Nigeria; the authors observed the Crystallographic Analysis and Environmental Fate Modeling of *Moringa Oleifera* Seed-Derived Silver Nanoparticles for Water Purification Applications. The ethical guidelines for plant materials are followed in the study for observation, identification & experimentation.

Funding
This research did not receive any external funding like specific grant from funding agencies in the public, commercial, or nonprofit sectors.

Data and materials availability
All data for this study have been included in the paper.

REFERENCES

1. Adebayo AA, Fagbenro OA. Growth performance and feed utilization of Oreochromis niloticus reared in tropical ponds. J Appl Aquac 2019; 31(3):245-258.
2. Adebayo AA, Oluwasola O, Adeniyi TA. Hydrological characteristics of Nigerian savanna rivers. J Hydrol Environ Res 2018; 6(2):112-125.
3. Alexander LE. X-ray diffraction methods in polymer science. Robert E. Krieger Publishing Company; 1979.
4. Ali I, Ahmed S, Khan MA, Shahid M, Hussain M, Ali S, Iqbal M, Ahmad F, Khan MZ, Ahmad S. The potential toxicity of chemically fabricated silver nanomaterials based on accumulation and histological changes in fish (Cyprinus carpio). Microsc Res Tech 2024; 87(10):2292-2300.
5. Amin N, Koelmans AA, Boxall ABA. Dynamic modeling of bioaccumulation and toxicity of engineered nanoparticles in aquatic food webs. Environ Sci Technol 2018; 52(15):8341-8352.
6. Aouf D, Khane Y, Fenniche F, Albukhaty S, Sulaiman GM, Khane S, Henni A, Zoukel A, Dizge N, Mohammed HA, Abomughaid MM. Biogenic silver nanoparticles of *Moringa oleifera* leaf extract: Characterization and photocatalytic application. Nanotechnol Rev 2024; 13(1).

7. Arnot JA, Gobas FAPC. A review of bioconcentration factor (BCF) and bioaccumulation factor (BAF) assessments for organic chemicals in aquatic organisms. Environ Rev 2006; 14(4):257-297.
8. Azároff LV. Elements of X-ray crystallography. McGraw-Hill; 1968.
9. Babakhani P, Bridge J, Doherty R, Phenrat T. Continuum-based models and concepts for the transport of nanoparticles in saturated porous media: A state-of-the-science review. Adv Colloid Interface Sci 2017; 246:75-104.
10. Bear J. Dynamics of fluids in porous media. Elsevier; 1972.
11. Borgonovo E, Plischke E. Sensitivity analysis: A review of recent advances. Eur J Oper Res 2016; 248(3):869-887.
12. Bradford SA, Torkzaban S. Colloid transport and retention in unsaturated porous media: A review of interface, pore, and transport processes. Vadose Zone J 2008; 7(2):667-681.
13. Bragg WH, Bragg WL. The reflection of X-rays by crystals. Proc R Soc Lond A 1913; 88(605):428-438.
14. Bucheli TD, Kasteel R. Modeling the environmental fate of nanoparticles. Environ Sci Technol 2010; 44(1):3-6.
15. Coelho N, Jacinto JP, Silva R, Soares JC, Pereira AS, Tavares P. Green synthesis and antibacterial activity of silver nanoparticles obtained from *Moringa oleifera* seed cake. Coatings 2023; 13(8):1439.
16. Cornelis G, Hund-Rinke K, Kuhlbusch T, van den Brink N, Nickel C. Fate and bioavailability of engineered nanoparticles in soils: A review. Crit Rev Environ Sci Technol 2014; 44(24):2720-2764.
17. Cornelis G, Kirby J, Beak D, McLaughlin M. Transport of silver nanoparticles in saturated columns of natural soils. Environ Sci Technol 2010; 44(4):1260-1266.
18. Crane M, Handy RD, Kille P. Bioaccumulation and toxicity of nanoparticles in aquatic ecosystems. Environ Toxicol Chem 2013; 32(5):963-972.
19. Crank J, Nicolson P. A practical method for numerical evaluation of solutions of partial differential equations of the heat-conduction type. Math Proc Camb Philos Soc 1947; 43(1):50-67.
20. Cullity BD, Stock SR. Elements of X-ray diffraction. 3rd ed. Pearson Education; 2014.
21. Cussler EL. Diffusion: Mass transfer in fluid systems. 3rd ed. Cambridge University Press; 2009.
22. Domenico PA, Schwartz FW. Physical and chemical hydrogeology. 2nd ed. John Wiley and Sons; 1998.
23. Elimelech M, Gregory J, Jia X, Williams RA. Particle deposition and aggregation: Measurement, modelling and simulation. Butterworth-Heinemann; 1995.
24. European Chemicals Agency. Guidance on information requirements and chemical safety assessment: Chapter R.11: PBT/vPvB assessment. ECHA; 2017.
25. Eze CC, Odunze AC. Environmental flow assessment for Nigerian rivers. Afr J Environ Sci Technol 2020; 14(5):125-138.
26. Federal Ministry of Water Resources. Water resources assessment of Nasarawa State. Federal Government of Nigeria; 2019.
27. Fetter CW. Applied hydrogeology. 4th ed. Prentice Hall; 2001.
28. Fischer HB, List EJ, Koh RCY, Imberger J, Brooks NH. Mixing in inland and coastal waters. Academic Press; 1979.
29. Freeze RA, Cherry JA. Groundwater. Prentice-Hall; 1979.
30. Frey HC, Patil SR. Identification and review of sensitivity analysis methods. Risk Anal 2002; 22(3):553-578.
31. Geitner NK, Zhao W, Wiesner MR. Environmental fate of engineered nanoparticles. In: Nanotechnology for environmental remediation. Springer; 2017. p. 45-78.
32. Gelhar LW, Welty C, Rehfeldt KR. A critical review of data on field-scale dispersion in aquifers. Water Resour Res 1992; 28(7):1955-1974.
33. Gobas FAPC, Mayer P, Parkerton TF, Burgess RM. On the role of bioaccumulation in the environmental risk assessment of chemical substances. Environ Toxicol Chem 2016; 35(10):2359-2372.
34. Hamby DM. A review of techniques for parameter sensitivity analysis of environmental models. Environ Monit Assess 1994; 32(2):135-154.
35. Hassan PB, Salih HA, Mohammed SA, Ahmed LA, Hamza HM, Hamad SM. Biosynthesis of silver and iron oxide nanoparticles using *Moringa oleifera* seed extract and their applications for water purification. J Univ Sulaimani 2025.
36. Helton JC, Davis FJ. Latin hypercube sampling and the propagation of uncertainty in analyses of complex systems. Reliab Eng Syst Saf 2003; 81(1):23-69.
37. Hillyer P, Giltrap M, Clements E. Probabilistic risk assessment of silver nanoparticles in aquatic food chains. Environ Sci Nano 2019; 6(4):1087-1099.
38. Hochella MF, Mogk DW, Ranville JF. Natural, incidental, and engineered nanomaterials and their impacts on the Earth system. Science 2019; 363(6434).
39. Holden PA, Gardea-Torresdey JL, Klaessig F, Turco RF, Mortimer M, Hund-Rinke K, Lyon DY. Considerations of environmentally relevant test conditions for improved evaluation of ecological hazards of engineered nanomaterials. Environ Sci Technol 2016; 50(12):6124-6145.
40. Holzwarth U, Gibson N. The Scherrer equation versus the 'Debye-Scherrer equation'. Nat Nanotechnol 2011; 6(9):534-536.

41. Hou WC, Jafvert CT. Photochemical transformation of aqueous silver nanoparticles: A mechanistic study. Environ Sci Technol 2019; 53(15):8631-8639.
42. Jenkins R, Snyder RL. Introduction to X-ray powder diffractometry. John Wiley and Sons; 1996.
43. Jiang C, Liu M, Wang Y. Effect of natural organic matter on the bioavailability of silver nanoparticles. Environ Pollut 2017; 231:804-813.
44. Johnson WP, Pazmino EF, Quintanilla CA. Colloid transport in saturated porous media: A review. Water Resour Res 2018; 54(5):3311-3338.
45. Kittel C. Introduction to solid state physics. 8th ed. John Wiley and Sons; 2005.
46. Kretzschmar R, Borkovec M, Grolimund D, Elimelech M. Mobile subsurface colloids and their role in contaminant transport. Adv Agron 1999; 66:121-193.
47. Landrum PF, Chapman PM, Neff J. Evaluating the bioaccumulation of nanoparticles in aquatic organisms. Environ Toxicol Chem 2012; 31(8):1695-1704.
48. Li Y, Zhang X, Wang L. Temperature dependence of silver nanoparticle dissolution. Environ Sci Process Impacts 2019; 21(8):1310-1319.
49. Liu J, Wang Z, Liu F. Silver nanoparticle photodegradation mechanisms. J Hazard Mater 2018; 347:178-186.
50. Louni R, Metcalfe CD, Helm PA. Bioaccumulation of engineered nanomaterials in aquatic food webs. Environ Sci Process Impacts 2020; 22(5):1143-1157.
51. Mackay D, Fraser A. Bioaccumulation of persistent organic chemicals: Mechanisms and models. Environ Pollut 2000; 110(3):375-391.
52. Mohamed A. Bionanoparticles from Moringa as antimicrobial activity and its application in water purification. J Curr Biomed Res 2021.
53. Molnar IL, Johnson WP, Gerhard JI, Willson CS, O'Carroll DM. Predicting colloid transport through saturated porous media: A critical review. Water Resour Res 2015; 51(9):6804-6845.
54. Morgan MG, Henrion M. Uncertainty: A guide to dealing with uncertainty in quantitative risk and policy analysis. Cambridge University Press; 1990.
55. Murugavel R, Wunderlich B. Crystallinity of polymers. Macromol Chem Phys 2012; 213(4):413-421.
56. Ng TY, Loo JK. Bioaccumulation modeling in aquatic organisms. Environ Sci Technol Lett 2018; 5(6):312-319.
57. Nichols JW, Schultz IR, Fitzsimmons PN. The role of gill physiology in the bioaccumulation of contaminants in fish. Aquat Toxicol 2015; 162:45-55.
58. Nigerian Meteorological Agency. Climate data for Nasarawa State. NIMET; 2020.
59. Norton J, Brown SL, Swinton J. Sensitivity analysis of environmental models: A review. Environ Model Softw 2006; 21(12):1735-1745.
60. Offiong OE, Okon AE. Hydrogeological assessment of shallow aquifers in the Benue Trough, Nigeria. Hydrogeol J 2019; 27(4):1345-1360.
61. Okomoda VT, Tiamiyu LO, Ataguba GA. Growth performance of Oreochromis niloticus in tropical aquaculture systems. Aquac Res 2018; 49(5):1892-1902.
62. Pan Y, Li H, Chen W. Size-dependent bioaccumulation of silver nanoparticles in zebrafish. Environ Sci Technol 2016; 50(14):7604-7612.
63. Park H, Kim S, Lee J. Crystallinity measurement of nanomaterials. Adv Mater Res 2007; 26-28:1045-1048.
64. Patterson AL. The Scherrer formula for X-ray particle size determination. Phys Rev 1939; 56(10):978-982.
65. Peijnenburg WJGM, Baalbergen E, Groot J. Modeling the fate and transport of nanoparticles in aquatic environments. Environ Toxicol Chem 2016; 35(9):2142-2150.
66. Petersen EJ, Henry TB, Zhao J. Bioaccumulation of nanomaterials in aquatic organisms. Environ Toxicol Chem 2018; 37(4):974-984.
67. Petosa AR, Jaisi DP, Quevedo IR, Elimelech M, Tufenkji N. Aggregation and deposition of engineered nanomaterials in aquatic environments: Role of physicochemical interactions. Environ Sci Technol 2010; 44(17):6532-6549.
68. Pratiwi DE, Side S, Nisa NAT. Synthesis of silver nanoparticles using *Moringa oleifera* L. leaf extract as bioreductor. Mater Sci Forum 2019:145-149.
69. Press WH, Teukolsky SA, Vetterling WT, Flannery BP. Numerical recipes: The art of scientific computing. 3rd ed. Cambridge University Press; 2007.
70. Rufai Abdul, Amangabara GT, Oguzie KL, Christopher EC, Nwachukwu JI. Predictive modeling and optimization of *Moringa oleifera* seed-derived silver nanoparticles (Mo-AgNPs) for multi-contaminant water purification in Doma, Nigeria. Sci Direct 2026; 17, 100294.
71. Rutherford JC. River mixing. John Wiley and Sons; 1994.
72. Sadia M, Ab'lah NN, Kamarozaman AS, Mehdi SGM, Channa IA, Taqvi SAA, Sidik NAC, Saidin S. Impact of crystallite size on surface roughness, antibacterial efficacy and hemocompatible properties of polycaprolactone incorporated *Moringa oleifera* extract and silver nanoparticles electrospun nanofibrous membrane. J Polym Eng 2025; 45(1):16-32.
73. Saltelli A, Ratto M, Andres T, Campolongo F, Cariboni J, Gatelli D, Saisana M, Tarantola S. Global sensitivity analysis: The primer. John Wiley and Sons; 2008.

74. Saltelli A, Tarantola S, Campolongo F, Ratto M. Sensitivity analysis in practice: A guide to assessing scientific models. John Wiley and Sons; 2004.
75. Scheidegger AE. On the theory of flow of miscible phases in porous media. Bull Int Assoc Sci Hydrol 1961; 6(2):13-18.
76. Scherrer P. Bestimmung der Größe und der inneren Struktur von Kolloidteilchen mittels Röntgenstrahlen. Nachr Ges Wiss Göttingen 1918; 26:98-100.
77. Selck H, Handy RD, Fernandes TF. Bioaccumulation and toxicity of engineered nanomaterials in aquatic ecosystems. Environ Toxicol Chem 2016; 35(10):2373-2381.
78. Sharma N, Singh R, Kumar A, Sharma P, Gupta S, Verma P, Singh SK, Sharma AK, Kumar V, Sharma D, Singh J. Behavioural changes, DNA damage and histological alterations in Labeo rohita fingerlings in response to organic-coated silver nanoparticles. Environ Sci Pollut Res Int 2024; 31(35):47789-47800.
79. Suárez-Oubiña C, Herbello-Hermelo P, Mallo N, Vázquez M, Cabaleiro S, Domínguez-González R, Moreda-Piñeiro A, Bermejo-Barrera P. Bioaccumulation and human risk assessment of inorganic nanoparticles in aquaculture species. Environ Sci Nano 2024; 11:2937-2947.
80. United Nations. Globally Harmonized System of Classification and Labelling of Chemicals (GHS). 8th ed. United Nations; 2019.
81. U.S. Environmental Protection Agency. Aquatic life criteria for silver. EPA; 2018.
82. Uvarov V, Popov I. Metrological characterization of X-ray diffraction methods for determination of crystallite size. Mater Charact 2007; 58(8-9):883-891.
83. Vered P, Bityutsky V, Kharchyshyn V, Zlochevskiy M. Toxicity, biotransformation and bioaccumulation of silver nanoparticles in laboratory conditions and aquatic ecosystems. OUCI 2023.
84. Wagner S, Gondikas A, Neubauer E. Natural organic matter and the bioavailability of silver nanoparticles. Environ Sci Technol 2014; 48(5):2622-2631.
85. Wang Y, Hu L, Zhang X. Transport of silver nanoparticles in iron-rich aquifer sediments. Environ Sci Technol Lett 2016; 3(12):422-427.
86. Wang Z, Lin D, Xing B. Size-dependent bioavailability of nanoparticles in aquatic organisms. Environ Sci Technol 2020; 54(16):10011-10020.
87. Welberry TR. Diffuse X-ray scattering and models of disorder. Oxford University Press; 2010.
88. Yu J, Liu F, Wang Z. Sedimentation and aggregation of silver nanoparticles in aquatic environments. Water Res 2021; 188:116542.
89. Zheng C, Bennett GD. Applied contaminant transport modeling. 2nd ed. John Wiley and Sons; 2002.
90. Zhou H, Xu C, Zhang Y. Photodegradation of silver nanoparticles in surface waters. Environ Sci Process Impacts 2020; 22(3):612-622.